# Regulation of invasion-associated actin dynamics by the *Chlamydia trachomatis* effectors TarP and TmeA

Matthew D. Romero and Rey A. Carabeo[1]

Department of Pathology and Microbiology, College of Medicine, University of Nebraska Medical Center, Omaha, NE

[1]Corresponding Author:
Department of Pathology and Microbiology
University of Nebraska Medical Center
985900 Nebraska Medical Center, Omaha, NE
Email: rey.carabeo@unmc.edu

**Key words: *Chlamydia* invasion, TarP, TmeA, formin, actin kinetics**

**Abstract:**

The obligate intracellular pathogen *Chlamydia trachomatis* manipulates the host actin cytoskeleton to assemble actin-rich structures that drive pathogen entry. The recent discovery of TmeA, which like TarP is an invasion-associated type III effector implicated in actin remodeling, raised questions regarding the nature of their functional interaction. Quantitative live-cell imaging of actin remodeling at invasion sites revealed differences in recruitment and turnover kinetics associated with TarP and TmeA pathways, with the former accounting for most of the robust actin dynamics at invasion sites. TarP-mediated recruitment of the actin nucleators formin and the Arp2/3 complex were crucial for rapid actin kinetics, generating a collaborative positive feedback loop that enhanced their respective actin-nucleating activities within invasion sites. In contrast, Fmn1 is neither recruited to invasion sites nor collaborates with Arp2/3 within the context of TmeA-associated actin recruitment. While the TarP-Fmn1-Arp2/3 signaling axis is responsible for the majority of actin dynamics, its inhibition had similar effects as deletion of TmeA on invasion efficiency, consistent with the proposed model that TarP and TmeA acting on different stages of the same invasion pathway.

**Summary Statement: Kinetic analysis of actin recruitment during *C. trachomatis* invasion reveals TarP as the major contributor relative to TmeA, via its ability to facilitate collaboration between actin nucleators Formin 1 and Arp2/3.**

35 **Introduction**

36 Infections caused by the obligate intracellular bacterium *Chlamydia trachomatis* are both the leading
37 cause of preventable blindness and the most prevalent bacterial form of sexually transmitted disease
38 worldwide (Malhotra et al., 2013). *Chlamydiae* are obligate intracellular pathogens that feature a
39 biphasic developmental cycle divided between metabolically inactive elementary bodies and the
40 vegetative reticulate bodies. Survival and replication occur in a membrane-bound vacuole known as an
41 inclusion, and therefore, gaining access to the intracellular environment is paramount (Bastidas et al.,
42 2013). Invading elementary bodies initially form a reversible electrostatic attachment onto heparin
43 sulfate proteoglycans on the host cell surface (Su et al., 1996; Zhang and Stephens, 1992). Shortly after,
44 *Chlamydia* engages and activates a multitude of host cell receptors while simultaneously delivering an
45 array of bacterial effectors by a type III secretion system (Chen et al., 2014; Fields et al., 2003; Gitsels et
46 al., 2019). Activation of host receptors and delivery of bacterial effectors during invasion allow
47 *Chlamydia* to exploit regulatory components of the actin cytoskeleton like Arp2/3, Rho GTPases, and
48 vinculin amongst others (Carabeo et al., 2007; Chen et al., 2014; Fadel and Eley, 2008; Gitsels et al.,
49 2019; Hower et al., 2009; Thwaites et al., 2015). By manipulating cytoskeletal regulators, *Chlamydia*
50 induces the formation of actin-rich microstructures on the cell surface that facilitate engulfment of the
51 pathogen (Carabeo et al., 2002; Caven and Carabeo, 2019). These structures can adopt a variety of
52 configurations, including phagocytic cups, membrane ruffles, filopodia, and hypertrophic microvilli
53 (Carabeo et al., 2007; Ford et al., 2018). A distinguishing characteristic of structures generated by
54 *Chlamydia* during invasion is their rapid and highly localized assembly (Carabeo et al., 2002). Whereas *S.*
55 *typhimurium* and *R. parkeri* recruit actin in a diffuse pattern over the span of 5-15 minutes (Francis et al.,
56 1993; Reed et al., 2014; Zhou et al., 1999), actin remodeling during *Chlamydia* invasion is highly localized
57 and recruitment and disassembly completed within two minutes (Carabeo et al., 2004).

58 Actin polymerization at the invasion site occurs is due in large part to the secretion of the
59 bacterial effectors TarP and TmeA, which jointly coordinate the assembly of a robust actin remodeling
60 network at *Chlamydia* entry sites. TarP and TmeA accomplish this task in part by their shared ability to
61 recruit the actin nucleator Arp2/3 during invasion. Arp2/3 is a complex of proteins which, upon
62 activation, enhances the rate of actin polymerization by nucleating branched actin filaments along a pre-
63 existing "mother" filament (Bailly et al., 1999; Mullins et al., 1998), and the resulting branched network
64 in turn increases the number of sites for Arp2/3 binding and branched nucleation (Higgs and Pollard,
65 1999). TarP and TmeA activate the Arp2/3 complex via downstream activation of the nucleation
66 promoting factors WAVE2 and N-WASP, respectively (Carabeo et al., 2007; Faris et al., 2020; Keb et al.,
67 2021; Lane et al., 2008). Both nucleation promoting factors have each been shown to be important for
68 *Chlamydia* engulfment, as targeted disruption of either protein attenuated pathogen uptake (Carabeo et
69 al., 2007; Faris et al., 2020; Keb et al., 2021). Furthermore, siRNA knockdown of WAVE2 prevented the
70 recruitment of actin at entry sites, highlighting the importance of TarP-associated Arp2/3 activation and
71 subsequent actin remodeling in *Chlamydia* pathogenesis (Carabeo et al., 2007).

72 The actin remodeling network generated by *Chlamydia* enable the assembly of invasion-
73 associated structures which are comprised entirely or in part by elongated bundles of filamentous actin.
74 A class of actin nucleators known as formins participate in the assembly of actin-rich structures by
75 facilitating rapid incorporation of actin monomers onto the barbed end of actin filaments (Shemesh and
76 Kozlov, 2007). In turn, these rapidly elongating filaments provide a highly localized protrusive force that
77 gives rise to actin-rich structures such as filopodia and hypertrophic microvilli (Fattouh et al., 2015; Kage
78 et al., 2017; Yang et al., 2007). Broadly, formins can be divided into two subclasses: diaphanous-related
79 formins (DRFs), which must be activated by Rho-GTPases before they can serve as actin nucleators, and
80 non-DRF formins, which do not require activation to participate in actin filament elongation (Baarlink et
81 al., 2010). Once activated, formins dimerize and incorporate monomeric actin onto the barbed end of an

82 actin filament. Formins have been demonstrated to participate in the invasion of bacterial pathogens
83 including *L. monocytogenes*, *S. typhimurium*, and *B. burgdorferi* (Boddy et al., 2018; Rengarajan et al.,
84 2016; Williams et al., 2018). Likewise, invading *C. trachomatis* is known to interact with hypertrophic
85 microvillar structures that are enriched with filamentous actin (Carabeo et al., 2002), raising the
86 possibility that *Chlamydia* also utilizes formins during invasion. In addition, formin and its homolog,
87 Diaphanous, along with components of the Arp2/3 complex were identified in an RNA interference
88 screen in Drosophila S2 cells as being important host factors in infection (Elwell et al., 2008).

89 Here, we implicate three formin family members (Fmn1, mDia1, and mDia2) as important
90 elements of *Chlamydia* invasion. We demonstrate that the recruitment of formin occurred via a TarP-
91 dependent and TmeA-independent process. An extensive yeast two-hybrid screen directed against TarP
92 failed to identify any of the three formin members, indicating that TarP-mediated formin recruitment
93 occurs via indirect interaction. Nevertheless, we observed that formin and the Arp2/3 complex were
94 simultaneously recruited during invasion, implying a functional interaction between these actin
95 nucleators. Indeed, the absence of either nucleator drastically reduced *Chlamydia* entry, which
96 correlated with a significant reduction in the rate of actin recruitment. These findings were recapitulated
97 using the pan-formin inhibitor SMIFH2 and the Arp2/3 inhibitor CK666. Notably, we found that
98 recruitment of Arp2/3 was dramatically diminished when Fmn1 is inhibited, and vice versa, indicating
99 that their respective recruitment depends on the actin network formed by the other. This
100 interdependent recruitment underpins enhanced actin recruitment kinetics, revealing a cross-
101 collaborative interaction which establishes a definitive mechanistic link between rapid actin kinetics and
102 efficient *Chlamydia* invasion. Quantification of actin kinetics also revealed the primacy of TarP signaling
103 as a key element of *Chlamydia* actin recruitment dynamics. Specifically, strains which lacked TarP
104 exhibited profound defects in the recruitment kinetics of actin, Formin 1, and Arp2/3, which were less
105 severe in strains lacking TmeA. Collectively, these findings point to TarP facilitating functional

106 collaboration between formins and Arp2/3 to promote the hallmark rapid actin recruitment and
107 turnover kinetics at the site of invasion.
108
109 **Results**
110 **TarP accounts for the majority of invasion-associated actin remodeling**
111 Rapid and robust recruitment of actin is a hallmark of *Chlamydia* invasion, which is coordinated in part
112 by the secreted effectors TarP and TmeA via their ability to recruit actin modulatory proteins during
113 invasion. Recently, it was shown that TarP and TmeA synergistically enhance the in-vitro rate of actin
114 polymerization (Keb et al., 2021). Genetic deletion of TarP (ΔTarP) or TmeA (ΔTmeA) attenuates
115 pathogen entry, which was rescued by cis-complementation of *ct456/tarp* (*cis*-TarP) or *ct694/tmea* (*cis*-
116 TmeA). On the basis of these observations, it was proposed that synergy between TmeA and TarP is an
117 important determinant of both robust actin kinetics and efficient invasion. To evaluate this claim, we
118 quantified the rate and intensity of actin recruitment at the entry sites of wild-type, single-knockout
119 (ΔTarP, ΔTmeA), cis-complemented (*cis*-TarP, *cis*-TmeA), or double-knockout (ΔTmeA/ΔTarP) *Chlamydia*
120 strains (Fig. 1, Video S1). Comparisons of actin recruitment between strains were derived by calculating
121 their respective fold recruitment values, which measures the fold increase of fluorescence intensity at
122 entry sites relative to the fluorescence intensity prior to the arrival of elementary bodies. Importantly,
123 background fluorescence signal was obtained from regions immediately outside of regions of *Chlamydia*
124 entry and subtracted from the specific fluorescence intensity obtained within the entry site. This
125 method of background subtraction accounts for local variations in fluorescence intensity, while
126 calculation of fold recruitment values accounts for potential variations in the expression levels of
127 fluorescent protein. Details of this process can be found in the supplementary data (Fig. S1).
128 Furthermore, we found that the recruitment profiles obtained from exogenously expressed GFP-actin

129 closely resembled the recruitment profile of endogenous actin stained with the far-red dye SiR (Fig. S2),
130 validating the use of either method to monitor actin dynamics.

131 While all strains retained the ability to recruit actin, we noted that the intensity of actin
132 recruitment was diminished upon deletion of TarP and/or TmeA (Fig. 1A,B). Wild-type and cis-
133 complemented strains of *Chlamydia* recruited actin at an average intensity of 18-fold above background,
134 which was reduced by 5-fold following TmeA deletion and 12-fold following TarP deletion. Interestingly,
135 the peak intensity of actin recruitment by the ΔTmeA/ΔTarP double-mutant strain (4.86-fold) was only
136 marginally reduced relative to ΔTarP (6.27-fold), suggesting that TmeA signaling alone is insufficient to
137 generate robust actin kinetics, and that TarP accounts for the majority of the actin signal intensity during
138 invasion. Despite this, and in agreement with earlier studies, we found that deletion of either TmeA or
139 TarP significantly reduced the efficiency of *Chlamydia* internalization (Wild-type=76.2%, ΔTmeA=50.4%,
140 ΔTarP=42.1%), and that deletion of both effectors worsened this defect (ΔTmeA/ΔTarP=29.6%) (Fig. 1C).
141 Collectively, these data indicate that strains lacking TarP and/or TmeA recruit actin suboptimally, which
142 is linked to poor invasion efficiency relative to either wild-type or *cis*-complemented strains.

143 In addition to reducing the intensity of actin recruitment, we also noted that the overall actin
144 recruitment profiles of ΔTarP and ΔTmeA strains differed from wild-type *Chlamydia*. In particular, both
145 ΔTarP and ΔTmeA/ΔTarP exhibit atypically transient actin recruitment, while ΔTmeA produces an
146 intermediate profile with slightly lower intensity and duration (Fig. 1B). These observations, coupled
147 with reduced invasion efficiency following TarP or TmeA deletion (Fig. 1C), are further proof of a link
148 between actin kinetics and invasion efficiency. We observed that the recruitment profile of actin
149 exhibited three distinct phases: i) recruitment, in which actin rapidly accumulates, ii) fast turnover, in
150 which actin is rapidly lost from the sites of invasion, likely through depolymerization and iii) slow
151 turnover, in which actin is gradually depolymerized over an extended time period (Fig. 1B). The
152 asynchrony between the time of EB arrival and the start of recruitment required a fixed temporal

153 reference point to enable quantification. For this, we plotted the first derivative values corresponding to
154 the velocity of recruitment and turnover for each timepoint and chose the first timepoint exhibiting
155 positive velocity as the start of recruitment. Further details regarding the criteria used to define
156 recruitment and turnover phases can be found in the supplemental data (Fig. S3).

157 To compare the kinetics of actin recruitment and turnover between conditions, we employed
158 linear regression to calculate the slope, representing the rate of recruitment and turnover for each
159 invasion event (Fig. S1,S3), and mapped these values onto a violin plot to visualize the distribution of
160 rates for each strain (Fig. 1D,E, Table S1). Deletion of either TmeA or TarP attenuated actin recruitment
161 kinetics by 2-fold and 5-fold, respectively, relative to wild-type *Chlamydia* (ΔTmeA=0.178 fold/sec,
162 ΔTarP=0.054 fold/sec). Actin kinetics were further restricted by simultaneous deletion of both TmeA and
163 TarP (ΔTmeA/ΔTarP=0.031 fold/sec), yielding a nearly 10-fold reduction in the rate of actin recruitment.
164 Altogether, these data suggest that optimal rapid actin recruitment is an effector-driven process that
165 relies on both TarP and TmeA. Furthermore, we observed that actin kinetics were more severely
166 attenuated in strains that lack TarP (ΔTarP, ΔTmeA/ΔTarP), suggesting that TarP is the major
167 determinant of actin recruitment kinetics, and that TmeA has a minor role.

168

169 **Formin 1 is involved in TarP-associated actin dynamics**

170 We investigated the basis for the greater impact of TarP on actin recruitment and tested the hypothesis
171 that TarP could be engaging multiple nucleators of actin polymerization. Formin family members, e.g.
172 formin and Diaphanous were identified in an RNA interference screen in Drosophila S2 cells for host
173 factors necessary for infection (Elwell et al., 2008). The need for actin remodeling during invasion raises
174 the possibility that the mammalian equivalents Fmn1, mDia1, and mDia2 are involved in this process.
175 Furthermore, analysis of formin recruitment within the context of the TarP- and TmeA-deficient mutant
176 strains may provide a basis for the greater role of TarP in actin remodeling dynamics.

177 Since multiple formin species are implicated as invasion-associated factors, we utilized
178 strategies which simultaneously impair their actin nucleating function to mitigate the possibility of
179 compensatory interactions. To this end, we exposed Cos7 cells to the pan-formin inhibitor SMIFH2 (10
180 μM), which prevents actin monomer binding onto formin species by occupying their conserved formin-
181 homology 2 (FH2) domain, and quantified *Chlamydia* invasion efficiency at 10 min post-infection. At this
182 dose, the reported off-target effects of SMIFH2 at 100 μM on myosin II activity was not observed based
183 on retention of myosin II-dependent focal adhesions and stress fibers in treated mock-infected Cos7
184 cells (Fig. S4) (Nishimura et al., 2021, 2). Quantitative invasion assay revealed a 39% decrease in invasion
185 efficiency following SMIFH2 treatment relative to mock-treated samples (Fig. 2A). Additionally,
186 simultaneous knockdown of Fmn1, mDia1, and mDia2 using a pooled esiRNA treatment (3x esiRNA)
187 reduced invasion efficiency by 45% compared to both mock- and scramble RNA-treated samples. We
188 note that individual knockdown of each formin species reduced invasion efficiency by approximately
189 20%, indicating functional compensation between formins (Fig. S5E).

190 Given that *Chlamydia* invasion is attenuated by depletion or inhibition of Fmn1, mDia1, and
191 mDia2, we chose to monitor the involvement of these proteins during pathogen entry. Time-lapse
192 images of Cos7 cells transfected to individually express fluorescence-tagged versions of Fmn1, mDia1,
193 and mDia2 were collected and assembled as videos, revealing that each of these proteins was recruited
194 at *Chlamydia* entry sites (Fig. 2B). Moreover, upon plotting their specific fluorescence intensity of over
195 time, we noted that each formin species exhibited rapid, robust, and transient recruitment (Fig. 2C).
196 Using the same method employed to quantify actin kinetics (Fig. 1D,E; Fig. S3), we compared the
197 recruitment and turnover kinetics of recruited formins (Fig. 2D,E). Although the rate of mDia2
198 recruitment (0.069 fold/sec) was marginally slower than Fmn1 (0.106 fold/sec) and mDia1 (0.096
199 fold/sec), we report that each formin species possesses largely comparable recruitment kinetics (Fig.
200 2D). A similar trend persists in their turnover kinetics, as Fmn1 (0.041 fold/sec), mDia1 (0.046 fold/sec)

201 and mDia2 (0.040 fold/sec) each had comparable turnover rates (Fig. 2E). Collectively, these data imply
202 that multiple formin species are recruited during *Chlamydia* invasion, that their recruitment supports
203 pathogen internalization, and that their activities are likely functionally redundant.

204 Provided the central importance of actin remodeling toward *Chlamydia* invasion, it is highly
205 probable that formins assist in pathogen entry by enhancing actin remodeling kinetics. To evaluate this
206 claim, we measured the effects of SMIFH2 treatment on actin dynamics within entry sites via time-lapse
207 live-cell imaging. Using the same methods described earlier (Fig. S1, S3), we quantified the specific
208 fluorescence intensity of GFP-actin recruited by *Chlamydia* in the presence and absence of SMIFH2 and
209 plotted this data as fold actin recruitment (Fig. 3A). Inhibition of formins yielded a substantial defect to
210 actin recruitment, reducing peak actin intensity by 11-fold (Mock = 19.69-fold vs. SMIFH2 = 8.99-fold).
211 Additionally, the actin recruitment kinetics generated by each experimental group differed significantly
212 in all phases, e.g. recruitment (0.285 fold/sec vs. 0.095 fold/sec), fast turnover (0.108 fold/sec vs. 0.031
213 fold/sec), and slow turnover (Fig. 3B,C). We were unable to evaluate whether simultaneous knockdown
214 of Fmn1, mDia1 and mDia2 via pooled esiRNA treatment yielded a comparable defect to actin kinetics,
215 as this treatment rendered cells highly susceptible to phototoxicity, and are thus unsuitable for live-cell
216 imaging (Fig. S5D). Nevertheless, these data indicate that the principal cause of reduced invasion
217 efficiency following disruption of formins is due to deficient actin remodeling.

218 We observed earlier in this study that strains which lack TarP (ΔTarP, ΔTmeA/ΔTarP) exhibited
219 more significant impediments in both actin recruitment and turnover than either wild-type or TmeA-
220 deficient (ΔTmeA) strains (Fig. 1B,D,E). One possible explanation for this difference may be that formins,
221 which enhance actin remodeling kinetics, are recruited in a TarP-specific manner. As such, we tested
222 whether the recruitment of formin was contingent upon the presence of TarP or TmeA (Fig. 3D-F),
223 focusing our investigation on the recruitment of Fmn1 since this protein was specifically identified in an
224 RNA interference screen of host factors necessary for infection (Elwell et al., 2008). We observed the

225 robust recruitment of Fmn1 at the entry sites of wild-type, *cis*-complemented, and ΔTmeA strains, which
226 was absent in ΔTarP and ΔTmeA/ΔTarP strains, suggesting that Fmn1 recruitment is TarP-dependent
227 (Fig. 3D). Interestingly, an extensive yeast two-hybrid screen directed against TarP failed to identify
228 Fmn1, mDia1, and mDia2, suggesting that formins do not directly interact with TarP (Table S1). As such,
229 it is likely that TarP-mediated recruitment of formins occurs indirectly, however the precise factors
230 which mediate this interaction remain unknown. TmeA deletion did not appreciably alter the
231 recruitment intensity of Fmn1 relative to either *cis*-TmeA or wild-type *Chlamydia* (wild-type=10.7-fold,
232 *cis*-TmeA=9.9-fold, ΔTmeA=8.5-fold), indicating that recruitment of Fmn1 is mediated primarily by TarP
233 and largely independent of TmeA. In further support of this, we found that Fmn1 recruitment kinetics
234 were not altered by TmeA deletion (wild-type=0.106 fold/sec vs. ΔTmeA=0.092 fold/sec) but were
235 reduced by over 10-fold following TarP deletion (ΔTarP=0.013 fold/sec) (Fig. 3E). Finally, we observed
236 that ΔTmeA EBs achieved a significantly higher Fmn1 turnover rate than wild-type *Chlamydia* (Wild-
237 type=0.041 fold/sec, ΔTmeA=0.070 fold/sec), while Fmn1 turnover was nearly negligible following TarP
238 deletion (ΔTarP=0.009 fold/sec) (Fig. 3F). Thus, we conclude that the involvement of Fmn1 toward
239 invasion-associated actin remodeling is TarP-specific, and that failure to recruit Fmn1 results in a
240 substantial defect to both actin kinetics and *Chlamydia* internalization.
241
242 **Arp3 recruitment and turnover are dependent on TarP and TmeA, respectively**
243 In addition to the presently established role of formins as enhancers of actin kinetics, it has also been
244 established that the actin branching protein Arp2/3 is recruited by *Chlamydia* to drive actin recruitment
245 (Lane et al., 2008). Indeed, a recent study suggested that TarP and TmeA signaling pathways form a
246 functional collaboration that enhances recruitment of Arp2/3 and increases the rate of actin
247 polymerization (Faris et al., 2020; Keb et al., 2021). As such, we monitored the recruitment of Arp3 fused
248 to either GFP or mCherry at the entry sites of wild-type, *cis*-complemented, or effector deletion strains

249 in order to assess the individual and combined contribution of the effectors on Arp2/3 recruitment (Fig.
250 4). We observed recruitment of Arp3 in all strains except for ΔTmeA/ΔTarP, indicating that Arp2/3
251 recruitment is contingent upon the presence of either TarP or TmeA (Fig. 4A,B). We noted that *cis*-TmeA
252 EBs required an additional 20 seconds to recruit Arp3 at a comparable intensity to either wild-type or
253 *cis*-TarP strains (Fig. 4B), which is consistent with the slight delay in peak actin intensity observed prior
254 (Fig. 1B). Surprisingly, TmeA deletion did not substantially alter the intensity of Arp3 recruitment,
255 whereas TarP deletion resulted in dim and transient Arp3 recruitment (Fig. 4B). In conjunction with the
256 absence of Arp3 recruitment in the ΔTmeA/ΔTarP strain, these data suggest that both TarP and TmeA
257 are independently capable of Arp3 recruitment. Nevertheless, the apparent differences between the
258 Arp3 recruitment profiles of ΔTarP and ΔTmeA are inconsistent with a synergistic interaction between
259 the effectors, instead indicating that Arp2/3 recruitment is primarily driven by TarP. However, we
260 observed that Arp3 recruitment at the entry sites of ΔTmeA EBs was visibly more transient than Arp3
261 recruitment in either *cis*-TmeA or wild-type strains, indicating a potential role for TmeA in promoting
262 stable recruitment of Arp2/3.

263 In order to clarify the respective contributions of TarP and TmeA toward Arp2/3 recruitment, we
264 monitored the kinetics of Arp3 recruitment and turnover for WT, ΔTarP, ΔTmeA, cis-TarP, cis-TmeA, and
265 ΔTarP/ΔTmeA strains (Fig. 4C,D). We noted that the recruitment kinetics of Arp3 were largely similar in
266 all strains except for ΔTarP and ΔTarP/ΔTmeA, the former recruiting Arp3 nearly 4-fold slower than wild-
267 type or *cis*-complemented strains (Wild-type=0.079 fold/sec, ΔTarP=0.020 fold/sec) (Fig. 4C). Consistent
268 with the delay in peak Arp3 intensity, *cis*-TmeA EBs possessed a slightly lower median Arp3 recruitment
269 rate (*cis*-TmeA=0.059 fold/sec) than wild-type or *cis*-TarP EBs, although their overall kinetics are largely
270 comparable. Finally, ΔTmeA EBs recruited Arp3 at a rate similar to wild-type or *cis*-TarP EBs (ΔTmeA=
271 0.091 fold/sec, *cis*-TarP= 0.095 fold/sec). Altogether, these data indicate that while TmeA is

272 independently capable of recruiting Arp2/3, it does so at a far slower rate than strains which contain
273 TarP. As such, we conclude that TarP is a key determinant of rapid Arp3 recruitment.

274 We found that the turnover rate of Arp3 was substantially higher at ΔTmeA entry sites
275 (ΔTmeA=0.091 fold/sec) than wild-type (0.035 fold/sec) or cis-TmeA (0.054 fold/sec) (Fig. 4D).
276 Furthermore, pairwise correlation analyses revealed that the Arp3 turnover rate of ΔTmeA EBs was
277 positively correlated with both its corresponding recruitment rate and its recruitment intensity, together
278 implying that rapid and intense Arp3 recruitment results in proportionally rapid Arp3 turnover (Fig. S9C).
279 Collectively, this demonstrates that the reduced invasion efficiency determined for ΔTmeA is due to
280 poor Arp2/3 retention at invasion sites resulting in attenuated actin kinetics. In other words, the inability
281 of the ΔTmeA strain to maintain an optimal pool of activated Arp2/3 at the site of invasion could
282 account for the observed two-fold reduction in the rate of actin recruitment. Meanwhile, TarP deletion
283 resulted in a drastic attenuation of Arp3 turnover kinetics relative to wild-type or *cis*-TarP strains (*cis*-
284 TarP=0.070 fold/sec, ΔTarP=0.023 fold/sec) (Fig. 4D). As with ΔTmeA, the significant reduction in actin
285 recruitment by the ΔTarP mutant could be due to the drastic reduction in Arp2/3 recruitment, coupled
286 with the loss of TarP-mediated recruitment of formins. In summary, these data indicate that TarP and
287 TmeA signaling are mutually important for optimal Arp2/3 kinetics, each regulating distinct attributes of
288 Arp2/3 recruitment. TarP signaling is associated with robust Arp2/3 recruitment, while TmeA signaling is
289 required Arp2/3 retention at entry sites. Coupled with the attenuated actin kinetics and poor invasion
290 efficiency of ΔTarP and ΔTmeA strains (Fig. 1), we conclude that efficient invasion is reliant upon the co-
291 regulation of Arp2/3 kinetics by TarP and TmeA.

292

293 **Formin collaboration with the Arp2/3 complex is necessary for robust actin dynamics and efficient**
294 ***Chlamydia* invasion**

295 Having established that TarP signaling is necessary for robust recruitment of Arp2/3 and Fmn1, we
296 opted to investigate the functional relationship between these two nucleators with regards to actin
297 dynamics and consequent invasion. Findings from a previously published RNA interference screen in
298 Drosophila S2 cells demonstrated that Arp2/3, formin, and Diaphanous are necessary for *Chlamydia*
299 infection, but if and how they function together remained obscure. To assess more accurately the
300 involvement of formin-mediated nucleation in actin dynamics and invasion efficiency, Arp2/3 complex
301 participation must be excluded. As such, we compared the data obtained from SMIFH2-treated cells
302 depicted earlier in the study (Fig. 3A-C) against Cos7 cells treated with the Arp2/3 inhibitor CK666
303 (100µM) or cells in which CK666 and SMIFH2 (100µM/10µM, respectively) were applied simultaneously.
304 Cos7 cells were pre-treated with inhibitors for 60 min prior to inoculation with *C. trachomatis* serovar L2
305 EBs (MOI=50), quantifying invasion efficiency at 10 min post-infection. We normalized our data to the
306 efficiency of invasion in absence of inhibitor in order to directly compare the effects of formin and/or
307 Arp2/3 inhibition on invasion. Loss of activity of either formin or Arp2/3 yielded a comparable
308 impediment to invasion, each reducing invasion efficiency by roughly 40%, while simultaneous inhibition
309 of formin and Arp2/3 reduced invasion efficiency by 60% (Fig. 5A). The importance of formins and
310 Arp2/3 toward efficient internalization are further underscored by the substantial 40-50% loss in
311 invasion efficiency upon simultaneous knockdown of formins (Fig. 2A) or individual knockdown of Arp2
312 (Fig. S6). Together, these data suggest that while formin and Arp2/3 activity are independently
313 important for invasion, their combined inactivation causes a more substantial inhibition of pathogen
314 entry.

315 We extended our earlier analysis of actin recruitment following the inhibition of formins (Fig.
316 3A-C) to include individual or co-inhibition of Arp2/3, quantifying the recruitment of GFP-actin in the
317 presence or absence of CK666 and SMIFH2 via time-lapse imaging of live Cos7 cells (Fig. 5B). *Chlamydia*
318 robustly recruited actin in the absence of inhibitor at an intensity of nearly 20-fold above background,

319 which was reduced by over 10-fold following application of SMIFH2 or CK666. Interestingly, dual
320 inhibition of formin and Arp2/3 yielded a form of actin recruitment that was substantially slower and
321 much more persistent, often failing to turn over throughout the duration of the experiment (Video S3).
322 In addition to exhibiting defects in actin recruitment intensity, we also found that the kinetics of actin
323 recruitment and turnover were disrupted by inhibition of formin or Arp2/3 (Fig. 5C,D). Specifically,
324 inhibition of formin or Arp2/3 comparably reduced the kinetics (fold/sec) of actin recruitment
325 (Mock=0.285, SMIFH2=0.082, CK666=0.072) and turnover (Mock=0.096, SMIFH2=0.026, CK666=0.031),
326 which was more severe upon co-inhibition of both nucleators. Altogether, these data indicate that
327 *Chlamydia* manipulates both formin and Arp2/3 to achieve robust and highly localized actin recruitment,
328 and that both nucleators must be functional to achieve efficient invasion. Additionally, via an unknown
329 mechanism, actin turnover kinetics also required both Arp2/3 and formin nucleators to be functional.

330 The observation that formin and Arp2/3 individually contributes to actin kinetics during invasion
331 raise the possibility that these nucleators act collaboratively, thereby enhancing the capacity of
332 *Chlamydia* to generate actin-rich invasion structures. If nucleator collaboration does indeed play a role
333 in invasion, we expect that both formin and Arp2/3 will be concurrently present within a single invasion
334 event. We observed that GFP-Fmn1 was robustly recruited during invasion, but unexpectedly in an
335 Arp2/3-dependent manner, in that CK666 treatment substantially reduced its presence at invasion sites
336 (Fig. 6A). Likewise, GFP-Arp3, which has been validated as a marker for the Arp2/3 complex (Welch et
337 al., 1997), was robustly recruited during invasion and also demonstrated reduced recruitment following
338 inhibition of formin (Fig. 6B). Altogether, this indicates that recruitment of Fmn1 and Arp2/3 are
339 reciprocally enhanced by their respective actin nucleating functions and subsequent actin
340 polymerization.

341 Next, we determined whether Fmn1 and Arp2/3 are co-recruited within individual invasion
342 events, thus providing the necessary context for nucleator collaboration. To do this, we co-expressed

343 GFP-Fmn1 and mCherry-Arp3 and measured the recruitment of both proteins during invasion by time-
344 lapse imaging followed by fluorescence quantification (Fig. 6C). We observed that all events we
345 monitored exhibited both Fmn1 and Arp3 accumulation, indicating that they are co-recruited by
346 *Chlamydia*. To measure the timing of their arrival, we normalized the intensity of recruitment to the
347 maximum fluorescence intensity of each protein at each timepoint, expecting that any delays in protein
348 recruitment would be represented by a shift in their recruitment profile. In contrast, we noted that the
349 recruitment profiles of both Fmn1 and Arp3 were remarkably similar and achieved maximal MFI at the
350 same timepoint, indicating that both proteins arrived at the entry site within 20 seconds of each other,
351 the temporal resolution of our imaging protocol. We confirmed these findings by collecting fixed-cell Z-
352 stacks of formin and Arp2/3 recruitment at *Chlamydia* entry sites, noting that both nucleators were
353 concurrently present at the base of invading elementary bodies (Fig. 6D). Given both the simultaneous
354 recruitment of Fmn1 and Arp2/3 and the reciprocal dependence of their respective activities for optimal
355 recruitment, we conclude that Fmn1 and Arp2/3 collaborate during invasion to promote actin
356 recruitment. This observation is particularly novel, given that there are no other instances of the
357 utilization of Fmn1 by bacterial pathogens within this collaborative context. Lastly, given the robust
358 recruitment of Fmn1, we were interested in whether other formin species such as DRFs could also
359 participate in nucleator collaboration. To this end, we found that mEmerald-mDia1 and mEmerald-
360 mDia2 were also recruited during invasion, and that their recruitment was impaired by Arp2/3 inhibition
361 (Fig. 6E, S7), suggesting that both DRF and non-DRF formins collaborate with Arp2/3 during invasion.
362 Additionally, the capacity of mDia1 and mDia2 to participate in nucleator collaboration further supports
363 our assertion that the multitude of formins recruited during invasion exhibit functional redundancy.

364 Using the same methodology to evaluate actin kinetics (Fig. 1D,E), we compared the recruitment
365 and turnover profiles of Fmn1 and Arp2/3 to more closely evaluate how inhibition of each protein alters
366 their recruitment and turnover dynamics during invasion. Compared to mock treatment, inhibition of

367 Fmn1 decreased the rate of Arp3 recruitment by 34 percent (Mock=0.079 fold/sec, SMIFH2=0.052
368 fold/sec), while inhibition of Arp2/3 reduced the rate of Fmn1 recruitment by 47 percent (Mock=0.106
369 fold/sec, CK666=0.056 fold/sec) (Fig. 6F). Together, this indicates that collaboration between the
370 activities of Fmn1 and Arp3 not only enhance the rate of actin recruitment (Fig. 5C), but also reciprocally
371 enhance their respective recruitment rates. As such, we conclude that Arp2/3-mediated actin branching
372 produces additional barbed-ends for Fmn1 binding; reciprocally, Fmn1 activity produces elongated actin
373 filaments which allow efficient incorporation of Arp2/3-nucleated branches into actin networks
374 generated by invading *Chlamydiae*. Fmn1-Arp2/3 collaboration was centered around TarP, but not
375 TmeA, on the basis that Fmn1 recruitment was TmeA-independent (Fig. 3D) and that the ΔTmeA mutant
376 (i.e. TarP-functional strain) exhibited similar cross-sensitivity toward nucleator inhibition as wild-type
377 *Chlamydia* (Fig. S8). These data collectively implicate Fmn1 in efficient invasion via its collaboration with
378 the Arp2/3 complex to mediate the hallmark robust actin dynamics. As an aside, the failure of TmeA to
379 recruit Fmn1, despite the presumed availability of barbed ends in Arp2/3-nucleated actin network is
380 interesting, and could indicate barbed end occupancy in TmeA-remodeled actin network, or that a TarP-
381 specific cofactor of Fmn1 is required for its recruitment.

382 Shifting our focus onto turnover, we found that CK666 treatment reduced the turnover rate of
383 Fmn1 by 4-fold compared to mock-treatment (Mock=0.041 fold/sec vs. CK666=0.009 fold/sec), while
384 SMIFH2 treatment did not significantly alter the rate of Arp3 turnover (Mock=0.019 fold/sec vs.
385 SMIFH2=0.024 fold/sec) (Fig. 6G). Furthermore, we found that the turnover rate of Fmn1 among
386 individual EBs was moderately correlated with its corresponding peak intensity (r=0.402), which was not
387 observed upon inhibition of Arp2/3 (r=0.074) (Fig. S9E). This discrepancy may be due to a relative lack of
388 Fmn1 binding sites coupled with poor actin turnover following inhibition of Arp2/3 (Fig. 5D), such that
389 the turnover rate of Fmn1 is dictated by binding site availability in inhibitor-treated cells. In contrast,
390 rapid turnover of Fmn1 in mock-treated cells is potentially due to the relative abundance of Fmn1

391 binding sites coupled with rapid actin turnover, such that Fmn1 turnover is likely dictated by actin
392 turnover dynamics. Meanwhile, we noted that SMIFH2 treatment did not alter the turnover rate of
393 Arp2/3 (Fig. 6F), nor did it exert any observable effect on the regulation of Arp2/3 turnover as indicated
394 by pairwise correlation analysis (Fig. S9E). Thus, we conclude that turnover of Fmn1 and Arp2/3 are
395 governed by different mechanisms, wherein Arp2/3 turnover occurs via a process that is independent of
396 Fmn1 activity.
397

398 **Discussion:**

399 In this study, we provide the first report of involvement of Fmn1, a member of formin nucleators, in
400 *Chlamydia* invasion, indicating that its principal role is to collaborate with TarP-associated Arp2/3
401 recruitment to mediate the hallmark robust actin dynamics observed at sites of EB uptake. While the
402 focus of this report is on actin recruitment, we also observed a correlation between reduced invasion
403 efficiency and actin turnover, indicating that optimal actin remodeling, including disassembly of the
404 actin network is an absolute requirement for efficient invasion. We provide ample evidence that TarP,
405 which facilitates Fmn1-Arp2/3 collaboration is the major determinant of actin recruitment. While its role
406 in invasion has been reported, here we were able to elucidate at the molecular level how it facilitates
407 invasion. Its function as a signaling platform manifests as a facilitator of Fmn1-Arp2/3 cooperation. TarP
408 appears to initiate Fmn1 and Arp2/3 recruitment, with accumulation facilitated by binding of nucleators
409 to the growing actin network, which in turn contribute to further actin polymerization. Thus, a self-
410 propagating model of recruitment of nucleators and actin explains the highly localized and robust actin
411 dynamics during invasion. A crucial missing element is how this cycle is terminated to initiate turnover.

412 Intracellular pathogens often target the actin cytoskeleton during entry, leading to robust actin
413 recruitment and subsequent formation of invasion-associated structures. Although *Chlamydia* has been
414 demonstrated to use several entry mechanisms to achieve internalization (filopodial capture, clathrin-
415 mediated endocytosis, macropinocytosis, membrane ruffling), we were unable to assign specific actin
416 dynamic profile to each mechanism. Therefore, while our study impressed the importance of TarP and
417 TmeA signaling toward optimal actin kinetics, we were unable to assign engulfment structures to a
418 specific actin dynamics profile. Likewise, further study is required to determine the role of formin and
419 Arp2/3 toward the assembly of each invasion-associated structure, and whether inhibition of either
420 actin nucleator prevents the utilization of a given entry mechanism.

421 We observed that the presence of *Chlamydia* effectors TarP and TmeA was associated with
422 rapid recruitment of actin, which was due in part to the collaboration between Fmn1 and Arp2/3. One
423 explanation for the high rate of recruitment observed in our study is the establishment of a positive
424 feedback loop, where actin branching by Arp2/3 and filament elongation by Fmn1 create additional
425 nodes for Arp2/3 and Fmn1 to bind (Fig. 7). Iterations of this process would account for both the high
426 recruitment rate of actin in addition to providing an explanation for why inhibition of Fmn1 and Arp2/3
427 comparably affect the recruitment rate of actin. However, this model does not immediately make
428 apparent why actin recruitment is transient, nor does it provide explanation for the slow and persistent
429 actin recruitment observed following inhibition of both formin and Arp2/3. Other host actin nucleators
430 such as SPIRE, APC, or Cordon bleu have not yet been identified in siRNA screens of invasion-associated
431 proteins, nor has any evidence of their involvement in *Chlamydia* invasion been given (Elwell et al.,
432 2016). Although TarP has been shown via pyrene-actin polymerization assay to serve as an actin
433 nucleator, it remains unknown whether it also performs this function in cell lines or *in vivo* (Jewett et al.,
434 2006). However, based on pharmacological inhibition of formin members and the Arp2/3 complex and
435 the drastic impairment of the kinetics of recruitment and turnover indicate that actin nucleation is
436 predominantly driven by host nucleators rather than TarP itself.

437 An interesting observation is the apparent exclusive relationship of Fmn1-Arp2/3 collaboration
438 with TarP. Why a TmeA-mediated Arp2/3 activation and ensuing actin nucleation and polymerization do
439 not support Fmn1 localization to invasion sites is unclear. We speculate that the actin network formed
440 by TmeA-N-WASP-Arp2/3 signaling is regulated by capping proteins that prevent Fmn1 access to barbed
441 ends, or that additional factors are involved in TarP-dependent Fmn1 recruitment. The role of capping
442 proteins have not been studied in detail in the context of *Chlamydia* invasion, but there are reports
443 indicating that SIK2 and CAP1 capping protein regulators contribute to invasion of *Salmonella enterica*
444 Typhimurium (Hahn et al., 2021; Misselwitz et al., 2011). In addition, the Drosophila homolog of the

445 capping protein regulator CARMIL1 was identified in the siRNA screen by Elwell et al. to be necessary for
446 *Chlamydia* infection of S2 cells (Elwell et al., 2008), thus raising the possibility that this protein regulates
447 not only actin dynamics, but also the stable recruitment of Fmn1 within entry sites.

448 While TarP-mediated signaling accounts for the majority of actin recruitment, this is not
449 reflected on invasion efficiency, where deletion of either TarP or TmeA resulted in similar levels of
450 reduction. It is important to note that invasion is evaluated using an assay that relies on antibody
451 accessibility. As such, even signaling pathways which yield only minor contributions to actin dynamics
452 could result in substantial defects in *Chlamydia* internalization. One possibility is that TmeA-independent
453 signaling is capable of robust initial recruitment of actin, but fails to provide the necessary signaling to
454 achieve completion of engulfment. This observation is supported by our data indicating that the
455 recruitment phase of TmeA-independent actin recruitment is comparable to wild-type *Chlamydia*,
456 whereas actin turnover in the absence of TmeA is much faster, suggesting its involvement in a later
457 stage of pathogen engulfment. Another possibility is that TarP and TmeA mediate different means of
458 invasion, suggesting that their respective roles in achieving pathogen uptake entail some level of non-
459 redundancy.

460 In addition to rapid actin recruitment, we also observed a two-phase actin turnover process
461 starting with a brief fast turnover phase (100-180 sec) followed by a prolonged slow turnover phase
462 (400-600 sec). The rate of actin turnover was reduced by deletion of either TmeA or TarP, or by
463 inhibition of either formin or Arp2/3, collectively indicating that rapid actin turnover is an effector-
464 driven process which is contingent upon the activity of actin nucleators. Although this process is
465 relatively understudied in intracellular bacterial invasion, actin turnover is of clear importance for
466 bacterial internalization. For instance, impairment or hyperactivation of the actin depolymerizing
467 protein ADF-cofilin restricts internalization of *S. enterica*, while overexpression of the ADF-cofilin kinase
468 LIMK reduced *L. monocytogenes* internalization (Bierne et al., 2001; Dai et al., 2004). In *C. burnetii* and *L.*

469 *monocytogenes*, time-course experiments tracking actin recruitment also demonstrated a clear spike in
470 actin recruitment followed by a two-phase rapid/residual turnover profile (Bierne et al., 2001; Meconi et
471 al., 1998). Thus, the actin turnover profile observed in our study may simply reflect normal actin
472 turnover dynamics, as opposed to being intrinsic to invading *Chlamydia*. Given the importance of host
473 actin depolymerization factors like gelsolin, ADF-cofilin and their regulators for efficient internalization
474 of other intracellular bacteria, it may be that such proteins are also responsible for actin turnover during
475 *Chlamydia* invasion (Maldonado-Contreras et al., 2017; Moffatt et al., 2012; Pieters et al., 2013; Zheng
476 et al., 2016). Indeed, an siRNA screen of *C. muridarum* invasion-associated proteins identified four actin
477 depolymerization factors, ADF-cofilin, cyclase associated protein (CAP), Coronin, and β-thymosin, each
478 of which reduced bacterial entry upon silencing (Fig. 7) (Elwell et al., 2008). Thus, one avenue for future
479 study is to characterize the role of ADF-cofilin and other actin depolymerization factors in *Chlamydia*
480 invasion, and detailed elucidation of their involvement would depend on investigations into actin
481 dynamics.

482 Overall, this study highlights the remarkable complexity of the interaction between invading
483 *Chlamydia* and the host cytoskeleton, identifying several novel interactions which culminate to support
484 rapid actin kinetics and efficient pathogen engulfment. In play are at least two effectors (TarP and
485 TmeA), signaling from accessory cell surface receptors, and the existing cross-regulatory machinery of
486 actin nucleation, polymerization, and turnover (Fig. 7). Adding to this complexity is the various
487 functional interactions between multiple formins/formin-like proteins with Arp2/3. Our data indicate
488 that filamentous and branched actin nucleation along with polymerization constitute a fundamental
489 interaction in which formins in general collaborate with Arp2/3 during invasion following their
490 recruitment by TarP and TmeA.

491

492 **Materials and Methods:**

493 **Cell and Bacterial Culture**

494 Green monkey kidney fibroblast-like (Cos7) cells and cervical adenocarcinoma epithelial (HeLa) cells
495 were cultured at 37˚C with 5% atmospheric CO2 in Dulbecco's Modified Eagle Medium (DMEM; Gibco,
496 Thermo Fisher Scientific, Waltham, MA, USA) supplemented with 10 µg/mL gentamicin, 2 mM L-
497 glutamine, and 10% (v/v) filter-sterilized fetal bovine serum (FBS). HeLa and Cos7 cells were cultured for
498 a maximum of 15 passages for all experiments. McCoy B mouse fibroblasts (originally from Dr. Harlan
499 Caldwell, NIH/NIAID) were cultured under comparable conditions. *Chlamydia trachomatis* serovar L2
500 (434/Bu) was propagated in McCoy cells and EBs were purified using a Gastrografin density gradient as
501 described previously (Caldwell et al., 1981).

502

503 **Reagents**

504 SMIFH2 (Tocris, Minneapolis, MN, USA) and CK666 (Sigma-Aldrich, St. Louis, MO, USA) were diluted
505 upon receipt to 100mM stock concentration in DMSO, S-nitro Blebbistatin (Cayman Chemical, Ann
506 Arbor, MI, USA) and Y-27632 (Cayman) were diluted to 10mM stock concentration in DMSO. All
507 inhibitors were dispensed into single use aliquots and stored at -20°C for no longer than 1 year after
508 receipt. SMIFH2 was diluted to a working concentration of 10µM (1:10000), S-nitro Blebbistatin and Y-
509 27632 were diluted to a working concentration of 10µM (1:1000), and CK666 was diluted to a working
510 concentration of 100µM (1:1000), each using supplemented DMEM as diluent.

511

512 **Invasion Assay**

513 Efficiency of *C. trachomatis* invasion in HeLa cells was performed as described previously (Carabeo et al.,
514 2002). Briefly, HeLa cells were seeded in 24-well plates containing acid-etched glass coverslips and
515 allowed to adhere overnight. Cells were pretreated with SMIFH2 (10µM) (Tocris, Minneapolis, MN,

516 USA), CK666 (100µM) (Sigma-Aldrich, St. Louis, MO, USA), or both, for 1 hour prior to infection.
517 Following inhibitor treatment, cells were infected with EBs derived from wild-type *C. trachomatis* L2
518 (434/Bu), *C. trachomatis* in which TarP, TmeA, or both were deleted by FRAEM (ΔTarP, ΔTmeA,
519 ΔTmeA/ΔTarP), or *C. trachomatis* in which TarP or TmeA expression was restored by *cis*-
520 complementation (*cis*-TarP, *cis*-TmeA) at MOI=50. EBs were allowed to attach to HeLa cells for 30 min at
521 4°C. Cells were rinsed with cold HBSS before temperature shift to 37°C by the addition of pre-warmed
522 DMEM + 10% FBS/2 mM L-glutamine and incubated at 37°C for 10 min. Cells were then washed with
523 cold HBSS containing 100 µg/mL heparin to remove any transiently adherent EBs before fixation in 4%
524 paraformaldehyde at room temperature for 15 min. Fixed cells were labeled with a mouse monoclonal
525 anti-*Chlamydia* LPS antibody (BioRad CF 6J12, Hercules, CA, USA), rinsed with 1x PBS, and fixed once
526 more in 4% paraformaldehyde for 10 min. Next, cells were permeabilized using 0.1% (w/v) Triton X-100
527 for 10 minutes at room temperature, rinsed with HBSS and labeled with rabbit polyclonal anti-
528 *Chlamydia trachomatis* antibody (Abcam ab252762, Cambridge, MA, USA). Cells were then rinsed in 1x
529 PBS and labeled with Alexa Fluor 488 anti-mouse (ThermoFisher #A28175, Waltham, MA, USA) and
530 Alexa Fluor 594 anti-rabbit (ThermoFisher #A-11012) IgG secondary antibodies. Coverslips were
531 mounted and observed on either a Leica DM500 (Leica, Allendale, NJ, USA) or Zeiss Axio Observer (Zeiss,
532 Dublin, CA, USA) epifluorescence microscopes. Percent invasion efficiency was quantified as total EBs
533 (red) – extracellular EBs (green)/total EBs (red) x 100%.
534

535 **Quantitative live cell imaging of *Chlamydia* invasion**

536 Cos7 cells were seeded onto Ibidi µ-Slide 8-well glass-bottomed chambers (Ibidi, Fitchburg, WI, USA) and
537 allowed to adhere overnight prior to transfection. Cells were transfected with fluorescent proteins as
538 indicated, using Lipofectamine 3000 (Thermo Fisher, Waltham, MA, USA) according to manufacturer
539 directions. Transfection was allowed to proceed overnight before replacing media with fresh DMEM +

540 10% FBS/2 mM L-glutamine and allowing protein expression to continue for a total of 24 hours post-
541 transfection. Transfection was verified on either a Leica SD6000 or Nikon CSU-W1 (Nikon, Melville, NY,
542 USA) spinning disk confocal microscope prior to application of DMEM containing SMIFH2 (10µM), CK666
543 (100µM) or both. Wells were individually infected with CMTPX-labeled wild-type *C. trachomatis* L2
544 (434/Bu), unless otherwise indicated, at MOI=20 and promptly imaged using a 60x objective (NA 1.40) in
545 a heated and humidified enclosure. Images were collected once every 20 seconds for 30 minutes, with
546 focal plane maintained using an infrared auto-focusing system. Upon completion of the imaging
547 protocol, the next well was infected and imaging repeated; mock-treated wells were imaged first to
548 allow inhibitor treatment sufficient time to achieve inhibition. Images were compiled into videos using
549 NIH ImageJ and analyzed to identify protein recruitment events. The mean fluorescence intensity (MFI)
550 of such events was measured for each timepoint alongside the local background MFI of a concentric
551 region immediately outside the recruitment event. Background MFI was subtracted from recruitment
552 MFI for each timepoint and converted into fold recruitment by dividing the MFI of each timepoint
553 against the baseline MFI, defined as the average MFI of five timepoints (100 sec) prior to the start of
554 recruitment.
555
556 **Fixed cell confocal imaging**
557 For Z-stacks of formin-1 and Arp3 colocalization, Cos7 cells were seeded onto Lab-Tek II 4-well glass
558 bottomed chambers (Nunc, Rochester, NY, USA) and allowed to adhere overnight. Cells were co-
559 transfected with Arp3-GFP and Fmn1-mCherry using Lipofecatmine 3000 according to manufacturer
560 directions. Transfection was allowed to proceed overnight before replacing media with fresh DMEM +
561 10% FBS/2 mM L-glutamine and allowing protein expression to continue for a total of 24 hours post-
562 transfection. Unstained density-gradient purified wild-type *C. trachomatis* elementary bodies were
563 added in cold growth medium at MOI=20 and allowed to sediment for 30 minutes in a 4°C shaking

564 incubator to synchronize infection. Invasion of elementary bodies was initiated by addition of
565 prewarmed growth media followed by incubation at 37˚C with 5% atmospheric CO2 for 20 minutes.
566 Invasion was halted by rinsing cells with cold HBSS twice before adding 4% paraformaldehyde to fix cells.
567 Next, cells were permeabilized using 0.1% (w/v) Triton X-100 for 10 minutes at room temperature,
568 rinsed with HBSS and labeled with rabbit polyclonal anti-*Chlamydia trachomatis* antibody (Abcam
569 ab252762, Cambridge, MA, USA). Cells were then rinsed in 1x PBS and labeled with Alexa Fluor 647
570 anti-rabbit (ThermoFisher #A-21245) IgG secondary antibody. Z-stacks were obtained using a Nikon CSU-
571 W1 confocal microscope, imaging 0.3 micron slices of GFP (Arp3), RFP (Fmn1), and Cy5 (*Chlamydia*)
572 fluorescence. Z-stacks were analyzed in ImageJ. For paxillin and vinculin staining, Cos7 cells were seeded
573 onto acid-etched glass coverslips placed within each well of a 24-well plate and allowed to adhere
574 overnight. Cells were treated with various concentrations of the myosin II inhibitor blebbistatin (5-
575 20μM), ROCK inhibitor Y27632 (5-20 μM), or pan-formin inhibitor SMIFH2 (5-40μM), incubating cells for
576 1 hour. Cells were then fixed in 4% paraformaldehyde for 15 minutes, permeabilized in 0.1% (w/v) Triton
577 X-100 for 10 minute, and probed with mouse monoclonal anti-vinculin (Abcam ab130007) and rabbit
578 monoclonal anti-paxillin (Abcam ab32084) antibodies. Cells were then rinsed in 1x PBS and labeled with
579 Alexa Fluor 488 anti-mouse (ThermoFisher #A28175) and Alexa Fluor 594 anti-rabbit (ThermoFisher #A-
580 11012) IgG secondary antibodies. Imaging of focal adhesion staining was conducted using a Nikon CSU-
581 W1 confocal microscope and images were assembled in ImageJ.
582
583 **RNA interference**
584 To obtain lysates for Western blotting, or RNA for qRT-PCR, HeLa cells were seeded onto tissue culture
585 treated 24-well plates and allowed to adhere overnight. Cells were transfected with 25-100 nM
586 Dharmacon SmartPool siRNAs directed against ACTR2 (Dharmacon L-012076-02-0005, Lafayette, CO,
587 USA), 100 nM Mission esiRNAs directed against FMN1 (Eupheria Biotech EHU089531, Dresden,

588 Germany), DIAPH1/mDia1 (Eupheria Biotech EHU109471), DIAPH3/mDia2 (Eupheria Biotech,
589 EHU090271), or 25-100 nM Trilencer-27 Universal scrambled negative control (Origene SR30004,
590 Rockville, MD, USA) using Lipofectamine RNAiMAX reagent (Thermo Fisher) according to manufacturer
591 directions. Incubation was allowed to proceed for 48 hours before lysing cells in either 2x Laemmli
592 buffer for Western blotting, or in TRIzol (Thermo Fisher) for RNA purification. For invasion assays
593 employing RNA interference, the transfection procedure was repeated as stated above for cells seeded
594 onto acid-etched glass coverslips, followed by processing cells for "inside-out" staining as described
595 earlier. For quantitative live-cell imaging following RNA interference, cells were seeded onto Ibidi µ-Slide
596 8-well glass-bottomed chambers and transfected using the method stated above, with some slight
597 modifications. Specifically, 24 hours after initial transfection with siRNA or esiRNA, cells were
598 transfected with GFP-actin using Lipofectamine 3000 reagent according to manufacturer directions and
599 allowed to incubate for an additional 24 hours. Transfected cells were then imaged according to the
600 protocol stated above for quantitative live-cell imaging.
601
602 **RNA isolation and quantitative RT-PCR**
603 HeLa cells were seeded onto 24-well plates and allowed to adhere overnight before transfection with
604 siRNA or esiRNA as detailed above. Cells were lysed using TRIzol reagent, incubating lysates for 5
605 minutes before transfer into a 1.5mL Eppendorf tube. Chloroform was added to tubes and shaken
606 vigorously before allowing tubes to resettle for an additional 5 minutes. Lysates were centrifuged at
607 10000x RPM for 5 minutes before transferring the top aqueous layer into a fresh Eppendorf tube.
608 Isopropanol was added to the aqueous layer, mixed gently, and incubated for 5 minutes prior to
609 centrifugation at 14000x RPM for 20 minutes. Liquid was decanted from tubes before addition of 75%
610 ethanol, followed by centrifugation at 9500x RPM for 5 minutes. Liquid was decanted from tubes and
611 pellets containing purified RNA were allowed to air-dry before addition of Tris-EDTA buffer to resuspend

612 RNA. cDNA was generated from purified RNA by PCR amplification using a SuperScript IV kit (Thermo
613 Fisher) according to manufacturer directions. cDNA was diluted 1:10 in nuclease-free $H_2O$ and added to
614 PowerUp SYBR Green Master Mix (Thermo Fisher) with specific qPCR primers diluted to 500 nM to
615 generate a master mix. Each experimental sample was assayed in triplicate and were run on an Applied
616 Biosystems QuantiStudio 3 Real Time PCR System using the following protocol: 1.) 50.0°C/2 min (x1), 2.)
617 95.0°C/10 min (x1), 3.) 95.0°C/15 sec (x40), 4.) 60.0°C/ 1 min (x1). Primers were subjected to dissociation
618 curve analysis to ensure that a single product was generated.
619
620 **Western Blotting**
621 Lysates generated as described above were resolved via SDS-PAGE in 10% polyacrylamide gels at 120
622 volts for 1.5 hours or until the dye front has begun to evacuate the bottom of the gel cassette. Gels were
623 transferred onto 0.45µM pore size nitrocellulose in 1x Towbin buffer + 10% methanol at 90 mA for 16
624 hours. Western blots were blocked in 5% bovine serum albumin for 1 hour, briefly rinsed in Tris buffered
625 saline + 0.1% Tween-20 (TBST) and incubated with appropriate primary antibody for 1 hour. Blots were
626 then washed three times for 5 minutes in TBST and probed with appropriate HRP-conjugated secondary
627 antibodies for 1 hour. Protein bands were resolved by chemiluminescence using Immobilon Western
628 HRP Substrate (Millipore Sigma, St Louis, MO, USA). Western blotting of myosin II phosphorylation was
629 conducted by densitometry analysis comparing the ratio of Phospho-Myosin Light Chain 2 (Thr18/Ser19)
630 antibody signal (Cell Signaling Technologies #3674, Danvers, MA, USA) to total Myosin Light Chain 2
631 antibody signal (Cell Signaling Technologies #3672), normalized against GAPDH-HRP antibody signal
632 (Abcam ab9385). Quantification of Arp2 expression via Western blotting was conducted by densitometry
633 analysis of anti-Arp2 antibody (Abcam ab47654) compared to β-actin loading control (Abcam ab49900)
634
635 **Plasmids and DNA preparation**

636 pEGFP-Actin–C1 (Heinzen et al., 1999) was provided by Dr Scott Grieshaber (University of Idaho). pEGFP-
637 N1-ACTR3 (Arp3-GFP) (Welch et al., 1997) was obtained from Dr Matthew Welch (Addgene plasmid
638 #8462). Arp3-pmCherryC1 (Taylor et al., 2011) was a gift from Christien Merrifield (Addgene plasmid
639 #27682). mEmerald-mDia1-N-14 (Addgene plasmid #54157), mEmerald-mDia2-N-14 (Addgene plasmid
640 #54159), and mRuby-LifeAct-7 (Addgene plasmid #54560) were gifted by Michael Davidson. pEGFPC2-
641 FmnIso1b (Zhou et al., 2006) was a gift from Philip Leder (Addgene plasmid #19320). pmCherryC1-
642 FmnIso1b was generated by a variant of Gibson assembly termed FastCloning (Li et al., 2011) and
643 included removal of EGFP from pEGFPC2-FmnIso1b and insertion of mCherry derived from Arp3-
644 pmCherryC1. Kanamycin-resistant transformants were selected and propagated for plasmid isolation
645 prior to sequence verification using an mCherry-Fwd sequencing primer supplied by Eurofins Genomics.
646 All plasmids were isolated using MiniPrep DNA isolation kits (Qiagen, Valencia, CA, USA) following a
647 variant protocol for DNA isolation termed MiraPrep (Pronobis et al., 2016). Following plasmid isolation,
648 the eluate was precipitated by addition of 3M sodium acetate (Invitrogen, Waltham, MA, USA) at 10%
649 (v/v) of eluate volume followed by addition of 250% (v/v) absolute ethanol calculated after addition of
650 sodium acetate. The mixture was incubated at 4°C overnight and centrifuged at 14,000×g for 15 minutes
651 at 4°C. Supernatant was removed and 70% ethanol was added, followed by centrifugation at 14,000×g
652 for 10 minutes at 4°C. Supernatant was removed once more, and precipitated DNA was resuspended in
653 nuclease-free $H_2O$. Primers for assembly of pmCherryC1-FmnIso1b are as follows: (pEGFPC2) Fwd: 5'
654 GGCGGAAGCGGAAGCATGGAAGGCACTCACTGCACC 3', Rev: 5' GCCCTTGCTCACCAT
655 GGTGGCGACCGGTAGCG 3'; (pmCherryC1) Fwd: 5' CTACCGGTCGCCACCATGGTGAGCAAGGGCGAGG 3',
656 Rev: 5' GTGAGTGCCTTCCATGCTTCCGCTTCCGCCG 3'.
657
658 **Graphs and statistical analysis**

659 Violin plots were made using the ggplot2 base package (version 3.1.0) as a component of the Tidyverse
660 package (https://cran.r-project.org/web/packages/tidyverse/index.html) in rStudio (version 4.0.3).
661 Wilcoxon ranked-sum tests to determine statistical significance between violin plots and tabulated
662 statistical analyses of violin plots were generated using base R statistics and the moments package
663 (version 0.14, https://cran.r-project.org/web/packages/moments/index.html) in rStudio and assembled
664 in Excel (Microsoft, Redmond, WA, USA). Linear regression analyses, recruitment plots, invasion assays,
665 and all statistics associated with these data (pairwise T-test, correlation coefficient, SEM) were
666 performed in Excel. All graphs were assembled using the free and open-source software GNU Image
667 Manipulation Program (GIMP, https://www.gimp.org/) and Inkscape (https://inkscape.org/). Proposed
668 model for collaboration (Fig. 6) was assembled using BioRender (https://app.biorender.com/).
669

670 **Acknowledgements**

671 We thank the members of the Carabeo lab for extensive feedback regarding the design, direction, and
672 analysis of the study. We thank Dr. Ken Fields (University of Kentucky College of Medicine) for the kind
673 gift of ΔTarP, ΔTmeA, ΔTmeA/ΔTarP and TarP/TmeA *cis*-complemented strains. This study was
674 supported by funding from the U.S. National Institutes of Health, National Institutes of Allergy and
675 Infectious Disease grant R01 AI065545 (R.A.C.). M.D.R. was further supported by a fellowship from the
676 Seattle Chapter of Achievement Rewards for College Scientists (ARCS). The contents and views
677 expressed within this publication are the sole responsibility of the authors.

678

679 **Author Contributions:**

680 M.D.R. and R.A.C. designed the experiments and wrote the manuscript. M.D.R. performed the
681 experiments, and M.D.R. and R.A.C. analyzed the data.

682

683 **Conflict of Interest**

684 The authors declare no conflict of interest.

685

686 **Data Availability**

687 Datasets regarding the raw data and analysis of invasion assays, fluorescence microscopy and associated
688 kinetic analyses are available in Dryad (https://doi.org/10.5061/dryad.0k6djhb0g).

689

690 **References:**


691 **Baarlink, C., Brandt, D. and Grosse, R.** (2010). SnapShot: Formins. *Cell* **142**, 172, 172.e1.

692 **Bailly, M., Macaluso, F., Cammer, M., Chan, A., Segall, J. E. and Condeelis, J. S.** (1999). Relationship
693 between Arp2/3 Complex and the Barbed Ends of Actin Filaments at the Leading Edge of
694 Carcinoma Cells after Epidermal Growth Factor Stimulation. *J Cell Biol* **145**, 331–345.

695 **Bastidas, R. J., Elwell, C. A., Engel, J. N. and Valdivia, R. H.** (2013). Chlamydial intracellular survival
696 strategies. *Cold Spring Harb Perspect Med* **3**, a010256.

697 **Bierne, H., Gouin, E., Roux, P., Caroni, P., Yin, H. L. and Cossart, P.** (2001). A role for cofilin and LIM
698 kinase in Listeria-induced phagocytosis. *J Cell Biol* **155**, 101–112.

699 **Boddy, K. C., Gao, A. D., Truong, D., Kim, M. S., Froese, C. D., Trimble, W. S. and Brumell, J. H.** (2018).
700 Septin-regulated actin dynamics promote Salmonella invasion of host cells. *Cell Microbiol* **20**,.

701 **Caldwell, H. D., Kromhout, J. and Schachter, J.** (1981). Purification and partial characterization of the
702 major outer membrane protein of Chlamydia trachomatis. *Infect Immun* **31**, 1161–1176.

703 **Carabeo, R. A., Grieshaber, S. S., Fischer, E. and Hackstadt, T.** (2002). Chlamydia trachomatis Induces
704 Remodeling of the Actin Cytoskeleton during Attachment and Entry into HeLa Cells. *Infect*
705 *Immun* **70**, 3793–3803.

706 **Carabeo, R. A., Grieshaber, S. S., Hasenkrug, A., Dooley, C. and Hackstadt, T.** (2004). Requirement for
707 the Rac GTPase in Chlamydia trachomatis invasion of non-phagocytic cells. *Traffic* **5**, 418–425.

708 **Carabeo, R. A., Dooley, C. A., Grieshaber, S. S. and Hackstadt, T.** (2007). Rac interacts with Abi-1 and
709 WAVE2 to promote an Arp2/3-dependent actin recruitment during chlamydial invasion. *Cellular*
710 *Microbiology* **9**, 2278–2288.

711 **Caven, L. and Carabeo, R. A.** (2019). Pathogenic Puppetry: Manipulation of the Host Actin Cytoskeleton
712 by Chlamydia Trachomatis.

713 **Chen, Y.-S., Bastidas, R. J., Saka, H. A., Carpenter, V. K., Richards, K. L., Plano, G. V. and Valdivia, R. H.**
714 (2014). The Chlamydia trachomatis type III secretion chaperone Slc1 engages multiple early
715 effectors, including TepP, a tyrosine-phosphorylated protein required for the recruitment of
716 CrkI-II to nascent inclusions and innate immune signaling. *PLoS Pathog* **10**, e1003954.

717 **Dai, S., Sarmiere, P. D., Wiggan, O., Bamburg, J. R. and Zhou, D.** (2004). Efficient Salmonella entry
718 requires activity cycles of host ADF and cofilin. *Cell Microbiol* **6**, 459–471.

719 **Elwell, C. A., Ceesay, A., Kim, J. H., Kalman, D. and Engel, J. N.** (2008). RNA Interference Screen
720 Identifies Abl Kinase and PDGFR Signaling in Chlamydia trachomatis Entry. *PLOS Pathogens* **4**,
721 e1000021.

722 **Elwell, C., Mirrashidi, K. and Engel, J.** (2016). Chlamydia cell biology and pathogenesis. *Nature Reviews*
723 *Microbiology* **14**, 385–400.

724 **Fadel, S. and Eley, A.** (2008). Differential glycosaminoglycan binding of Chlamydia trachomatis OmcB
725 protein from serovars E and LGV. *J Med Microbiol* **57**, 1058–1061.

726 **Faris, R., McCullough, A., Andersen, S. E., Moninger, T. O. and Weber, M. M.** (2020). The Chlamydia
727 trachomatis secreted effector TmeA hijacks the N-WASP-ARP2/3 actin remodeling axis to
728 facilitate cellular invasion. *PLOS Pathogens* **16**, e1008878.

729 **Fattouh, R., Kwon, H., Czuczman, M. A., Copeland, J. W., Pelletier, L., Quinlan, M. E., Muise, A. M.,**
730 **Higgins, D. E. and Brumell, J. H.** (2015). The Diaphanous-Related Formins Promote Protrusion
731 Formation and Cell-to-Cell Spread of Listeria monocytogenes. *The Journal of Infectious Diseases*
732 **211**, 1185–1195.

733 **Fields, K. A., Mead, D. J., Dooley, C. A. and Hackstadt, T.** (2003). Chlamydia trachomatis type III
734 secretion: evidence for a functional apparatus during early-cycle development. *Mol Microbiol*
735 **48**, 671–683.

736 **Ford, C., Nans, A., Boucrot, E. and Hayward, R. D.** (2018). Chlamydia exploits filopodial capture and a
737 macropinocytosis-like pathway for host cell entry. *PLOS Pathogens* **14**, e1007051.

738 **Francis, C. L., Ryan, T. A., Jones, B. D., Smith, S. J. and Falkow, S.** (1993). Ruffles induced by Salmonella
739 and other stimuli direct macropinocytosis of bacteria. *Nature* **364**, 639–642.

740 **Gitsels, A., Sanders, N. and Vanrompay, D.** (2019). Chlamydial Infection From Outside to Inside. *Front*
741 *Microbiol* **10**,.

742 **Hahn, M., Covarrubias-Pinto, A., Herhaus, L., Satpathy, S., Klann, K., Boyle, K. B., Münch, C.,**
743 **Rajalingam, K., Randow, F., Choudhary, C., et al.** (2021). SIK2 orchestrates actin-dependent host
744 response upon *Salmonella* infection. *Proc. Natl. Acad. Sci. U.S.A.* **118**, e2024144118.

745 **Heinzen, R. A., Grieshaber, S. S., Van Kirk, L. S. and Devin, C. J.** (1999). Dynamics of Actin-Based
746 Movement by Rickettsia rickettsii in Vero Cells. *Infect Immun* **67**, 4201–4207.

747 **Higgs, H. N. and Pollard, T. D.** (1999). Regulation of Actin Polymerization by Arp2/3 Complex and
748 WASp/Scar Proteins *. *Journal of Biological Chemistry* **274**, 32531–32534.

749 **Hower, S., Wolf, K. and Fields, K. A.** (2009). Evidence that CT694 is a novel Chlamydia trachomatis T3S
750 substrate capable of functioning during invasion or early cycle development. *Mol Microbiol* **72**,
751 1423–1437.

752 **Jewett, T. J., Fischer, E. R., Mead, D. J. and Hackstadt, T.** (2006). Chlamydial TARP is a bacterial
753 nucleator of actin. *Proc Natl Acad Sci U S A* **103**, 15599–15604.

754 **Kage, F., Winterhoff, M., Dimchev, V., Mueller, J., Thalheim, T., Freise, A., Brühmann, S., Kollasser, J.,**
755 **Block, J., Dimchev, G., et al.** (2017). FMNL formins boost lamellipodial force generation. *Nat*
756 *Commun* **8**, 14832.

757 **Keb, G., Ferrell, J., Scanlon, K. R., Jewett, T. J. and Fields, K. A.** (2021). Chlamydia trachomatis TmeA
758 Directly Activates N-WASP To Promote Actin Polymerization and Functions Synergistically with
759 TarP during Invasion. *mBio* **12**, e02861-20.

760 **Lane, B. J., Mutchler, C., Al Khodor, S., Grieshaber, S. S. and Carabeo, R. A.** (2008). Chlamydial Entry
761 Involves TARP Binding of Guanine Nucleotide Exchange Factors. *PLOS Pathogens* **4**, e1000014.

762 **Li, C., Wen, A., Shen, B., Lu, J., Huang, Y. and Chang, Y.** (2011). FastCloning: a highly simplified,
763 purification-free, sequence- and ligation-independent PCR cloning method. *BMC Biotechnology*
764 **11**, 92.

765 **Maldonado-Contreras, A., Birtley, J. R., Boll, E., Zhao, Y., Mumy, K. L., Toscano, J., Ayehunie, S.,**
766 **Reinecker, H.-C., Stern, L. J. and McCormick, B. A.** (2017). Shigella depends on SepA to
767 destabilize the intestinal epithelial integrity via cofilin activation. *Gut Microbes* **8**, 544–560.

768 **Malhotra, M., Sood, S., Mukherjee, A., Muralidhar, S. and Bala, M.** (2013). Genital Chlamydia
769 trachomatis: An update. *Indian J Med Res* **138**, 303–316.

770 **Meconi, S., Jacomo, V., Boquet, P., Raoult, D., Mege, J.-L. and Capo, C.** (1998). Coxiella burnetii Induces
771 Reorganization of the Actin Cytoskeleton in Human Monocytes. *Infection and Immunity* **66**,
772 5527–5533.

773 **Misselwitz, B., Dilling, S., Vonaesch, P., Sacher, R., Snijder, B., Schlumberger, M., Rout, S., Stark, M.,**
774 **von Mering, C., Pelkmans, L., et al.** (2011). RNAi screen of Salmonella invasion shows role of
775 COPI in membrane targeting of cholesterol and Cdc42. *Mol Syst Biol* **7**, 474.

776 **Moffatt, C. E., Inaba, H., Hirano, T. and Lamont, R. J.** (2012). Porphyromonas gingivalis SerB-mediated
777 dephosphorylation of host cell cofilin modulates invasion efficiency. *Cellular Microbiology* **14**,
778 577–588.

779 **Mullins, R. D., Heuser, J. A. and Pollard, T. D.** (1998). The interaction of Arp2/3 complex with actin:
780 Nucleation, high affinity pointed end capping, and formation of branching networks of
781 filaments. *PNAS* **95**, 6181–6186.

782 **Nishimura, Y., Shi, S., Zhang, F., Liu, R., Takagi, Y., Bershadsky, A. D., Viasnoff, V. and Sellers, J. R.**
783 (2021). The formin inhibitor SMIFH2 inhibits members of the myosin superfamily. *J Cell Sci* **134**,
784 jcs253708.

785 **Pieters, J., Müller, P. and Jayachandran, R.** (2013). On guard: coronin proteins in innate and adaptive
786 immunity. *Nature Reviews Immunology* **13**, 510–518.

787 **Pronobis, M. I., Deuitch, N. and Peifer, M.** (2016). The Miraprep: A Protocol that Uses a Miniprep Kit
788 and Provides Maxiprep Yields. *PLOS ONE* **11**, e0160509.

789 **Reed, S. C. O., Lamason, R. L., Risca, V. I., Abernathy, E. and Welch, M. D.** (2014). Rickettsia Actin-Based
790 Motility Occurs in Distinct Phases Mediated by Different Actin Nucleators. *Current Biology* **24**,
791 98–103.

792 **Rengarajan, M., Hayer, A. and Theriot, J. A.** (2016). Endothelial Cells Use a Formin-Dependent
793 Phagocytosis-Like Process to Internalize the Bacterium Listeria monocytogenes. *PLOS Pathogens*
794 **12**, e1005603.

795 **Shemesh, T. and Kozlov, M. M.** (2007). Actin Polymerization upon Processive Capping by Formin: A
796 Model for Slowing and Acceleration. *Biophys J* **92**, 1512–1521.

797 **Su, H., Raymond, L., Rockey, D. D., Fischer, E., Hackstadt, T. and Caldwell, H. D.** (1996). A recombinant
798 Chlamydia trachomatis major outer membrane protein binds to heparan sulfate receptors on
799 epithelial cells. *Proc Natl Acad Sci U S A* **93**, 11143–11148.

800 **Taylor, M. J., Perrais, D. and Merrifield, C. J.** (2011). A high precision survey of the molecular dynamics
801 of mammalian clathrin-mediated endocytosis. *PLoS Biol* **9**, e1000604.

802 **Thwaites, T. R., Pedrosa, A. T., Peacock, T. P. and Carabeo, R. A.** (2015). Vinculin Interacts with the
803 Chlamydia Effector TarP Via a Tripartite Vinculin Binding Domain to Mediate Actin Recruitment
804 and Assembly at the Plasma Membrane. *Front. Cell. Infect. Microbiol.* **5**,.

805 **Welch, M. D., DePace, A. H., Verma, S., Iwamatsu, A. and Mitchison, T. J.** (1997). The Human Arp2/3
806 Complex Is Composed of Evolutionarily Conserved Subunits and Is Localized to Cellular Regions
807 of Dynamic Actin Filament Assembly. *J Cell Biol* **138**, 375–384.

808 **Williams, S. K., Weiner, Z. P. and Gilmore, R. D.** (2018). Human neuroglial cells internalize Borrelia
809 burgdorferi by coiling phagocytosis mediated by Daam1. *PLoS One* **13**, e0197413.

810 **Yang, C., Czech, L., Gerboth, S., Kojima, S., Scita, G. and Svitkina, T.** (2007). Novel roles of formin mDia2
811 in lamellipodia and filopodia formation in motile cells. *PLoS Biol* **5**, e317.

812 **Zhang, J. P. and Stephens, R. S.** (1992). Mechanism of C. trachomatis attachment to eukaryotic host
813 cells. *Cell* **69**, 861–869.

814 **Zheng, K., Kitazato, K., Wang, Y. and He, Z.** (2016). Pathogenic microbes manipulate cofilin activity to
815 subvert actin cytoskeleton. *Critical Reviews in Microbiology* **42**, 677–695.

816 **Zhou, D., Mooseker, M. S. and Galán, J. E.** (1999). An invasion-associated Salmonella protein modulates
817 the actin-bundling activity of plastin. *PNAS* **96**, 10176–10181.

818 **Zhou, F., Leder, P. and Martin, S. S.** (2006). Formin-1 protein associates with microtubules through a
819 peptide domain encoded by exon-2. *Exp Cell Res* **312**, 1119–1126.

820

821 **Figure 1: Deletion of TarP and TmeA impair invasion and attenuates kinetics of actin recruitment and**
822 **turnover.**

823 (A,B) Cos7 cells were transfected with Actin-GFP or mRuby-LifeAct for 24 hours prior to infection with
824 wild-type, single-knockout (ΔTarP, ΔTmeA), cis-complemented (*cis*-TarP, *cis*-TmeA), or double-knockout
825 (ΔTmeA/ΔTarP) *Chlamydia* strains at MOI=20. Infection was monitored by live-cell confocal microscopy
826 using a Nikon CSU-W1 spinning disk microscope, obtaining images every 20 seconds for 30 minutes to
827 identify sites exhibiting actin recruitment. (B) Recruitment events were isolated by selecting regions
828 containing invading *Chlamydia* and elevated actin fluorescence. Background fluorescence was
829 subtracted, and fold recruitment was calculated as a function of the fold increase in mean fluorescence
830 intensity of recruited actin compared to basal actin fluorescence. Detailed visualization of this process
831 can be found in Fig. S1. Data is displayed as mean fold recruitment for each timepoint +/- SEM compiled
832 from a minimum N=18 recruitment events. (C) HeLa cells were infected with each *Chlamydia* strain
833 indicated above at MOI=50 and stained using the "in-and-out" method which distinguishes non-
834 internalized EBs from total cell-associated EBs, as described in Materials and Methods. Results were
835 normalized against mean invasion efficiency of wild-type *Chlamydia* and plotted as normalized mean +/-
836 SEM. Data was collected from 15 fields, with each field containing an average of 100 *Chlamydiae*.
837 Statistical significance was determined by T- test. (D,E) All actin recruitment events used to create the
838 averaged plot shown previously (Fig. 1B) were individually divided into recruitment and turnover phases
839 (Fig. S3). Individual rates of (D) recruitment and (E) turnover were plotted on a violin plot with inset
840 boxplot, reporting the median rate +/- SD for each strain tested. Violin plots contain a minimum N=18
841 individual rates. Statistical significance was determined by Wilcoxon Rank-sum. All data are
842 representative of at least 3 independent experiments, * $P \leq 0.05$, ** $P \leq 0.01$, *** $P \leq 0.001$.

843

844 **Figure 2: Multiple formin species are recruited during invasion and promote *Chlamydia***
845 **internalization.**

846 (A) Expression of Fmn1, mDia1, and mDia2 within HeLa cells was simultaneously repressed via RNA
847 interference, using a pooled mixture containing 100ng of three esiRNAs (3x esiRNA) targeting transcripts
848 of each aforementioned gene. Pooled esiRNA or scramble RNA control was transfected into HeLa cells
849 and incubated for 48 hours prior to infection with wild-type *C. trachomatis* elementary bodies at
850 MOI=50. Concurrently, HeLa cells were mock-treated or treated with the pan-formin inhibitor SMIFH2
851 (10μM) for 1 hour prior to infection (MOI=50). Infected cells were fixed with 4% paraformaldehyde at 10
852 minutes post infection and stained to distinguish internalized elementary bodies using the method
853 described earlier (Fig. 1C). Results were normalized against mean invasion efficiency of mock-treated
854 *Chlamydia* and plotted as normalized mean +/- SEM. Data was collected from 15 fields, with each field
855 containing an average of 100 *Chlamydiae*. Statistical significance was determined by T- test. (B,C) Cos7
856 cells were transfected with GFP-Fmn1, mEmerald-mDia1, or mEmerald-mDia2 for 24 hours prior to
857 infection with wild-type *Chlamydia* stained with red-fluorescent dye (CMTPX) at MOI=20. Infection was
858 monitored by live-cell confocal microscopy, obtaining images every 20 seconds for 30 minutes to
859 identify sites exhibiting formin recruitment. Fluorescence intensity of formin recruitment was measured
860 as described earlier (Fig. 1B) and plotted as mean fold recruitment for each timepoint +/- SEM compiled
861 from a minimum N=15 recruitment events. (D,E) Recruitment and turnover kinetics were analyzed for
862 Fmn1, mDia1, and mDia2 recruitment curves using the same methodology described in Fig. 1D,E. Violin
863 plots contain a minimum N=15 individual rates, reporting the median rate +/- SD. Statistical significance
864 was determined by Wilcoxon Rank-sum. All data are representative of at least 3 independent
865 experiments, * $P \leq 0.05$, ** $P \leq 0.01$, *** $P \leq 0.001$.

866

867 **Figure 3: TarP-dependent recruitment of formin is required for rapid actin kinetics.**

868 (A,B) Cos7 cells were transfected with Actin-GFP for 24 hours prior to application of the pan-formin
869 inhibitor SMIFH2 (10μM) or mock DMSO control for 1 hour, followed by infection with wild-type CMTPX-

870 stained *Chlamydia* (MOI=20). Infection was monitored by live-cell confocal microscopy, and fluorescence
871 intensity of actin recruitment was measured using methods described earlier (Fig. 1A,B), plotting the
872 mean fold recruitment for each timepoint +/- SEM compiled from a minimum N=16 recruitment events.
873 (B,C) Actin recruitment and turnover kinetics were analyzed for both mock and SMIFH2 treated groups
874 using the same methodology described in Fig. 1D,E. Violin plots contain a minimum N=16 individual
875 rates, reporting the median rate +/- SD. (D) Cos7 cells were transfected with Fmn1-GFP or Fmn1-
876 mCherry for 24 hours prior to infection with the indicated *Chlamydia* strains at MOI=20. Infection was
877 monitored by live-cell confocal microscopy using a Nikon CSU-W1 spinning disk microscope, obtaining
878 images every 20 seconds for 30 minutes to identify sites exhibiting Fmn1 recruitment. Fluorescence
879 intensity of Fmn1 recruitment was measured as described earlier (Fig. 1B) and plotted as mean fold
880 recruitment for each timepoint +/- SEM compiled from a minimum N=17 recruitment events. (E,F)
881 Kinetics of Fmn1 recruitment and turnover were analyzed for each strain indicated above using the
882 same methodology described earlier. Violin plots contain a minimum N=17 individual rates, reporting
883 the median rate +/- SD. Statistical significance was determined by Wilcoxon Rank-sum. All data are
884 representative of at least 3 independent experiments, * $P \leq 0.05$, ** $P \leq 0.01$, *** $P \leq 0.001$.

885

886 **Figure 4: Arp3 recruitment and turnover are dependent on TarP and TmeA, respectively**

887 (A,B) Cos7 cells were transfected with Arp3-GFP or Arp3-mCherry for 24 hours prior to infection with
888 wild-type, single-knockout (ΔTarP, ΔTmeA), cis-complemented (*cis*-TarP, *cis*-TmeA), or double-knockout
889 (ΔTmeA/ΔTarP) *Chlamydia* strains at MOI=20. Infection was monitored by live-cell confocal microscopy
890 using a Nikon CSU-W1 spinning disk microscope, obtaining images every 20 seconds for 30 minutes to
891 identify sites exhibiting Arp3 recruitment. (B) Fluorescence intensity of Arp3 recruitment was measured
892 as described earlier (Fig. 1B) and plotted as mean fold recruitment for each timepoint +/- SEM compiled
893 from a minimum N=12 recruitment events. (C,D) Kinetics of Arp3 recruitment and turnover were

894 analyzed for each strain indicated above using the same methodology described in Fig. 1D,E. Violin plots
895 contain a minimum N=12 individual rates, reporting the median rate +/- SD. Statistical significance was
896 determined by Wilcoxon Rank-sum. All data are representative of at least 3 independent experiments, *
897 P ≤ 0.05, ** P ≤ 0.01, *** P ≤ 0.001.
898
899 **Figure 5. Formin and Arp2/3 activity are necessary for efficient invasion and optimal actin recruitment**
900 **kinetics.**
901 (A) HeLa cells were mock-treated or pretreated with inhibitors against formin (10µM SMIFH2), Arp2/3
902 (100µM CK666) or both (CK+SMI) for 1hr, infected with *C. trachomatis* serovar L2 at MOI=50 and stained
903 using the "in-and-out" method described earlier. Results were normalized against mean invasion
904 efficiency of mock treated cells (Untreated mean = 49% invasion efficiency) and plotted as normalized
905 mean +/- SEM. Data was collected from 20 fields, with each field containing an average of 108
906 Chlamydiae. Statistical significance was determined by T- test. (B) Cos7 cells were transfected with GFP-
907 actin or a GFP empty vector plasmid for 24hrs prior to mock-treatment or pretreatment with 10µM
908 SMIFH2, 100µM CK666, or both for 1hr. Transfected cells were infected with *Chlamydia* stained with
909 CMTPX at MOI=20 and imaged by quantitative live-cell imaging, collecting images every 20 seconds for
910 30 minutes. Fluorescence intensity of GFP-actin recruitment was measured as described earlier (Fig. 1B)
911 and plotted as mean fold recruitment for each timepoint +/- SEM compiled from a minimum N=16
912 recruitment events. (C, D) Kinetics of GFP-actin recruitment and turnover were analyzed for each
913 condition using the same methodology described in Fig. 1D,E. Violin plots contain a minimum N=16
914 individual rates, reporting the median rate +/- SD. Statistical significance was determined by Wilcoxon
915 Rank-sum. All data are representative of at least 3 independent experiments, * P ≤ 0.05, ** P ≤ 0.01, ***
916 P ≤ 0.001.
917

918 **Figure 6: Formin 1 and Arp3 collaboration enhances recruitment kinetics at entry sites.**

919 (A,B) Cos7 cells were transfected with (A) GFP-formin 1 isoform 1B (GFP-Fmn1) or (B) GFP-Arp3 for 24
920 hours prior to mock-treatment or pretreatment with 10µM SMIFH2 or 100µM CK666 for 1 hour.
921 Quantitative live-cell imaging of invading CMTPX- labeled *Chlamydia* (MOI=20) was performed as
922 described in Fig. 1B. Briefly, images were acquired once every 20 seconds for 30 minutes and assembled
923 into videos. MFI of recruitment events were obtained, and background fluorescence subtracted, before
924 quantifying and plotting the fold recruitment values +/- SEM of Fmn1 or Arp3 for each timepoint. Data
925 was compiled from a minimum N=16 recruitment events. (C) Cos7 cells were co-transfected with GFP-
926 Fmn1 and mCherry-Arp3 for 24 hours prior to infection with unlabeled *C. trachomatis* (MOI=20)
927 followed by quantitative live-cell imaging of invasion. Image acquisition and processing was performed
928 as described above with a few modifications. Since CMTPX and mCherry-Arp3 fluorescence overlap,
929 unlabeled *Chlamydia* was used, thus recruitment events are defined simply as regions containing
930 elevated GFP-Fmn1 fluorescence compared to local background. MFI of both GFP-Fmn1 and mCherry-
931 Arp3 were obtained from the recruitment ROI, and background was subtracted from both GFP and RFP
932 channels independently. Maximal MFI was derived from both channels and used to normalize
933 fluorescence as percent maximal MFI for each protein. Normalized MFI values for each timepoint were
934 compiled from 33 events, plotting mean %Max MFI +/- SEM. (D) Cos7 cells were co-transfected with
935 GFP-Arp3 and Fmn1-mCherry for 24 hours before synchronized infection with *C. trachomatis* (MOI=20).
936 Invasion was halted at 20 minutes post-infection and *Chlamydia* stained via immunofluorescence. Cells
937 were analyzed by confocal microscopy, obtaining Z-stacks of formin and Arp2/3 recruitment at sites of
938 *Chlamydia* invasion. (E) Recruitment of mEmerald-mDia1 and mEmerald-mDia2 was monitored in the
939 presence and absence of 100µM CK666 using the method described above for monitoring the
940 recruitment of GFP-Fmn1 and GFP-Arp3. Data is displayed as mean fold recruitment for each timepoint
941 +/- SEM compiled from a minimum N=22 recruitment events. (F,G) Kinetics of Fmn1 and Arp3

942 recruitment and turnover were analyzed in the presence and absence of 100µM CK666 or 10µM
943 SMIFH2, respectively, using the same methodology described in Fig. 1D,E. Violin plots contain a
944 minimum N=16 individual rates, reporting the median rate +/- SD. Statistical significance was
945 determined by Wilcoxon Rank-sum. All data are representative of at least 3 independent experiments, *
946 $P \leq 0.05$, ** $P \leq 0.01$, *** $P \leq 0.001$.
947
948 **Figure 7: Proposed model for collaboration between formin and Arp2/3 and subsequent rapid actin**
949 **recruitment and turnover.**
950 *C. trachomatis* engages and activates a multitude of host receptors whose activation is linked to the
951 recruitment of formin, Arp2/3, and actin in non-invasion contexts. It is currently unknown whether
952 receptor activation contributes to actin remodeling during invasion. Concurrent with receptor
953 engagement, *Chlamydia* secretes the effectors TmeA and TarP via Type III secretion system; each
954 effector activates Arp2/3 through N-WASP or WAVE2, respectively. Deletion of either TarP or TmeA
955 attenuated the kinetics of Arp2/3 recruitment and turnover, which may reflect a failure to optimally
956 activate and integrate Arp2/3 into actin networks. In addition to recruiting Arp2/3, TarP was also shown
957 to be essential for the recruitment of Fmn1 and may also function to recruit mDia1 and/or mDia2 via
958 signaling through Rac1. Collaboration between Arp2/3 and formin via their respective actin branching
959 and elongating activities increases the rate of actin recruitment. Inhibition of Arp2/3 by CK666 or formin
960 by SMIFH2 prevents this collaboration and constrains the actin network into either filamentous-only or
961 branching-only networks.
962
963 **Figure S1: Detailed image analysis throughput used to evaluate the intensity of protein recruitment.**
964 Quantitative live-cell imaging of fluorescent protein recruitment was utilized several times in various
965 conditions throughout this study, necessitating a consistent throughput to facilitate direct comparison.

966 (A) Videos of *Chlamydia* invasion were assembled following image acquisition in ImageJ and analyzed to
967 identify protein recruitment events. Protein recruitment was defined by regions exhibiting high
968 fluorescence intensity (Yellow) as compared to local background (Red). When possible, fluorescent
969 *Chlamydia* (CMTPX-*Chlamydia,* GFP-*Chlamydia,* RFP-*Chlamydia*) were used to ensure recruitment was
970 specific to an invading bacterium. Regions-of-interest (ROIs) specific to recruitment were selected to
971 include the entirety of the recruitment event across all timepoints, and a concentric region immediately
972 outside of this region was selected as a background ROI. (B) The mean fluorescence intensity (MFI) of
973 both recruitment and background ROI was obtained for each timepoint. (C) Background MFI was
974 subtracted from recruitment MFI to normalize for local variations in fluorescence intensity and for
975 photobleaching during image acquisition. Fold recruitment was calculated by dividing the MFI of each
976 timepoint by the average MFI of 5 timepoints (100 sec, yellow dots) prior to the start of recruitment,
977 defined as the point in which recruitment velocity begins to increase. (D) Fold recruitment values were
978 plotted against time for each recruitment event. Multiple events were aligned according to peak
979 recruitment for each event before calculating the mean fold recruitment across all events.

980

981 **Figure S2: Endogenous SiR-stained actin recruits comparably to exogenously expressed GFP-actin.**
982 (A) Recruitment of GFP-actin at sites of CMTPX-*Chlamydia* entry (Fig. 3A) were represented as a time-
983 course montage to depict actin recruitment dynamics. (B) Cos7 cell monolayers were treated with 1µM
984 SiR-actin alongside the broad-spectrum efflux pump inhibitor Verapamil (10µM) for 30 minutes prior to
985 infection with CMTPX-*Chlamydia* (MOI=20). Recruitment of SiR-actin at *Chlamydia* entry sites was
986 monitored as described earlier (Fig. 3A) and represented as a time-course montage. (C) Fluorescence
987 intensity of actin recruitment was measured as described earlier (Fig. 3A) and plotted as mean fold
988 recruitment for each timepoint +/- SEM compiled from a minimum N=10 recruitment events.

989

990 **Figure S3: Entry and exit points for each phase determined by velocity of recruitment and turnover.**
991 Each event used to generate the protein recruitment plots shown throughout this study were divided
992 into three phases, recruitment, fast turnover, and slow turnover, in order to study their kinetics. Entry
993 and exit points for these phases was determined by plotting the first derivative value (i.e., velocity) of
994 protein recruitment for each timepoint. Start of recruitment was defined as 20 seconds after velocity
995 began to increase (t=160s, dark green), since this timepoint was more consistently associated with
996 recruitment across events than the preceding timepoint (t=140s). End of recruitment was defined as the
997 timepoint immediately prior to when velocity is at its minimum, or 20 seconds prior to Vmin (t=240s,
998 light green). Start of fast turnover was defined as the timepoint associated with Vmin (t=260s, dark
999 gray), and the end of fast turnover was defined as the point in which turnover ceased to decelerate
1000 (t=340s, light gray). Start of slow turnover was defined as the timepoint immediately following the end
1001 of fast turnover (t=360s, dark orange), and terminated at the timepoint prior to when velocity crosses
1002 the x-intercept (t=760s, light orange). This analysis was conducted for all events independently and was
1003 used as the basis for linear regression analysis to determine the rate (slope) of recruitment, fast
1004 turnover, and slow turnover across multiple proteins, strains, and inhibitor treatment conditions.

1005

1006 **Figure S4: SMIFH2 does not inhibit myosin superfamily proteins at relatively low concentrations.**
1007 Cos7 cells were treated with (A) the nonmuscle myosin II inhibitor s-nitro blebbistatin, (B) the rho-
1008 associated protein kinase (ROCK) inhibitor Y27632, or (C) the pan-formin inhibitor SMIFH2 at various
1009 concentrations for 1 hour. Cells were probed with anti-vinculin and anti-paxillin antibodies and stained
1010 using fluorescent secondary antibodies to identify the integrity of focal adhesions following inhibitor
1011 treatment. (D) Cos7 cells were treated with blebbistatin, Y27632, or SMIFH2 at various concentrations
1012 for 1 hour prior to lysis in Laemmli buffer. Lysates were resolved by SDS-PAGE followed by Western

1013 blotting and probed with antibodies reactive against phospho-myosin light chain 2 (p-MLC2
1014 Thr18/Ser19), total myosin light chain 2 (t-MLC2), and GAPDH. (E) p-MLC2 abundance was quantified for
1015 each sample by ratiometric analysis of p-MLC2 intensity versus total MLC2 intensity, with each condition
1016 normalized against mock treatment. The concentration of SMIFH2 utilized to inhibit formins throughout
1017 this study (10µM) did not prevent the formation of intact focal adhesions or restrict phosphorylation of
1018 MLC2.

1019

1020 **Figure S5: RNA interference of formin species attenuates invasion efficiency and causes phototoxicity.**
1021 (A-C) HeLa cells were transfected with 100ng esiRNA to repress expression of Fmn1, mDia1, mDia2
1022 either individually or collectively, using a pooled mixture of all three esiRNAs (3x esiRNA), alongside a
1023 scramble RNA control series. Expression levels of (A) Fmn1, (B) mDia1, or (C) mDia2 were quantified by
1024 qRT-PCR, normalized against scramble RNA control. (D) Cos7 cells were transfected with a pooled
1025 mixture of 100ng each Fmn1, mDia1, and mDia2 esiRNAs (3x esiRNA) for 24 hours, at which point cells
1026 were transfected with GFP-actin and incubated for an additional 24 hours. Transfected cells were
1027 infected with CMTPX-*Chlamydia* (MOI=20), monitoring invasion via live-cell confocal microscopy,
1028 collecting images every 20 seconds for 30 minutes. Quantification of actin recruitment was prevented
1029 due to cell death as a result of increased phototoxicity following esiRNA treatment. (E) Cos7 cells were
1030 transfected with esiRNA or scramble RNA control as described above, prior to infection with wild-type *C.*
1031 *trachomatis* elementary bodies (MOI=50), halting infection by application of 4% paraformaldehyde at 10
1032 minutes post infection. Cells were stained to distinguish internalized elementary bodies using the
1033 method described earlier (Fig. 1C). Results were normalized against mean invasion efficiency of mock-
1034 treated *Chlamydia* and plotted as normalized mean +/- SEM. Data was collected from 15 fields, with
1035 each field containing an average of 72 *Chlamydiae*. Statistical significance was determined by T- test.

1036

1037 **Figure S6: RNA interference of Arp2 expression reduces invasion efficiency and actin recruitment.**
1038 (A) HeLa cells were transfected with concentrations of Arp2 siRNA ranging from 25nM to 100nM for 48
1039 or 72 hours, alongside 100nM scramble RNA control. Cells were lysed in 2x Laemmli buffer and resolved
1040 via Western blot, probing blots with antibodies against Arp2, in addition to β-actin as a loading control.
1041 (B) Band intensity of Arp2 was measured for each condition and normalized against the intensity of β-
1042 actin, plotting Arp2 expression levels as percent expression relative to Arp2 expression in untreated
1043 cells. (C) HeLa cells were transfected with 25nm siRNA against Arp2 or 25nM scramble RNA for 48 hours
1044 prior to infection with wild-type *C. trachomatis* elementary bodies (MOI=50), halting infection by
1045 application of 4% paraformaldehyde at 10 minutes post infection. Cells were stained to distinguish
1046 internalized elementary bodies using the method described earlier (Fig. 1C). Results were normalized
1047 against mean invasion efficiency of mock-treated *Chlamydia* and plotted as normalized mean +/- SEM.
1048 Statistical significance was determined by T- test. (D) Cos7 cells were transfected with 25nm siRNA
1049 against Arp2 or 25nM scramble RNA for 24 hours, at which point cells were transfected with GFP-actin
1050 and incubated for an additional 24 hours. Transfected cells were infected with CMTPX-*Chlamydia*
1051 (MOI=20), monitoring invasion via live-cell confocal microscopy, collecting images every 20 seconds for
1052 30 minutes. Fluorescence intensity of actin recruitment was measured as described earlier (Fig. 1B) and
1053 plotted as mean fold recruitment for each timepoint +/- SEM compiled from a minimum N=10
1054 recruitment events.

1055

1056 **Figure S7: Kinetics of mDia1 and mDia2 recruitment and turnover are attenuated by Arp2/3 inhibition.**
1057 All mDia1/2 recruitment events used to create the averaged plot shown previously (Fig. 2D) were
1058 individually divided into recruitment, fast turnover and slow turnover phases (Fig. S3). Individual rates of
1059 (A) recruitment and (B) fast turnover were plotted on a violin plot with inset boxplot, reporting the
1060 median rate +/- SD for each inhibitor treatment condition. Violin plots contain a minimum N=22

1061 individual rates. Statistical significance was determined by Wilcoxon Rank-sum. Data are representative
1062 of at least 3 independent experiments, ** P ≤ 0.01, *** P ≤ 0.001.
1063
1064 **Figure S8: TmeA-independent actin recruitment is driven by formin and Arp2/3 activity.**
1065 (A) Cos7 cells were transfected with GFP-actin for 24hrs prior to mock-treatment or pretreatment with
1066 10µM SMIFH2, 100µM CK666, or both for 1hr. Transfected cells were infected with ΔTmeA *Chlamydia*
1067 EBs at MOI=20 and imaged by quantitative live-cell imaging, collecting images every 20 seconds for 30
1068 minutes. Fluorescence intensity of GFP-actin recruitment was measured as described earlier (Fig. 1B)
1069 and plotted as mean fold recruitment for each timepoint +/- SEM compiled from a minimum N=16
1070 recruitment events. (B, C) Kinetics of GFP-actin recruitment and turnover were analyzed for each
1071 condition using the same methodology described in Fig. 1D,E. Violin plots contain a minimum N=16
1072 individual rates, reporting the median rate +/- SD. Statistical significance was determined by Wilcoxon
1073 Rank-sum. All data are representative of at least 3 independent experiments, * P ≤ 0.05, ** P ≤ 0.01, ***
1074 P ≤ 0.001.
1075
1076 **Figure S9: Pairwise correlation analyses of protein recruitment, turnover, and intensity.**
1077 Recruitment and kinetics data from (A) Fig. 1, (B) Fig. 3, (C) Fig. 4, (D) Fig.5, (E) Fig. 6, and (F) Fig. S7 were
1078 compiled and analyzed by pairwise correlation analysis to identify the extent of co-regulation between
1079 protein recruitment, turnover, and intensity for each protein and condition.
1080
1081 **Table S1: Proteins identified as TarP-interacting proteins via yeast two-hybrid screen.**
1082 The pB27-TarP(1-1005)-LexA bait plasmid was used to screen a cDNA library consisting of randomly
1083 primed HeLa cell protein baits using a proprietary high-throughput yeast-two hybrid screening service
1084 (Hybrigenics ULTImate Y2H Screen) to identify host proteins which interact with TarP.

1085

1086 **Movie S1: Representative video of fluorescent protein recruitment during *Chlamydia* invasion**

1087 Cos7 cells were transfected with plasmids expressing various GFP-fusion proteins for 24 hours prior to
1088 infection with CMTPX-stained *C. trachomatis* EBs (MOI=20). Bacterial adhesion and entry was monitored
1089 by live-cell imaging using a spinning disk confocal microscope (Nikon CSU-W1 or Leica SD6000 AF),
1090 obtaining images every 20 seconds for 30 minutes to identify sites exhibiting protein recruitment.
1091 Images were assembled into videos in ImageJ and annotated to highlight recruitment events. The
1092 representative video shown here depicts GFP-actin recruitment at sites where CMTPX-*Chlamydia*
1093 contacts the host cell (arrows). Similar videos were assembled for all proteins monitored throughout the
1094 study, each yielding recruitment events that exhibit tight localization around fluorescent *Chlamydia*,
1095 enabling straightforward quantification of recruitment intensity and duration (Figs. S1-3).

1096

1097 **Movie S2: GFP expressed via empty vector plasmid is not recruited during *Chlamydia* invasion.**

1098 Cos7 cells were transfected with a GFP-empty vector plasmid for 24 hours prior to infection with
1099 CMTPX-stained *C. trachomatis* EBs (MOI=20). Infection was monitored via live-cell confocal microscopy
1100 as described earlier. Images were assembled into videos in ImageJ and annotated to highlight sites
1101 where CMTPX-*Chlamydia* contact the host cell (arrows). Absence of GFP-empty vector recruitment at
1102 sites of entry demonstrate that recruitment is specific to the host protein fused to GFP.

1103

1104 **Movie S3: Co-inhibition of formin and Arp2/3 yields abnormal actin recruitment kinetics around**
1105 **invading *Chlamydia***

1106 Cos7 cells were transfected with GFP-actin 24hrs prior to pretreatment with 10µM SMIFH2 and 100µM
1107 CK666 for 1hr. Transfected cells were infected with unlabeled *Chlamydia* at MOI=20 and imaged by

1108 quantitative live-cell imaging, collecting images every 20 seconds for 30 minutes. Images were

1109 assembled into videos in ImageJ and annotated to highlight recruitment events (arrows).

1110

# Figure 1

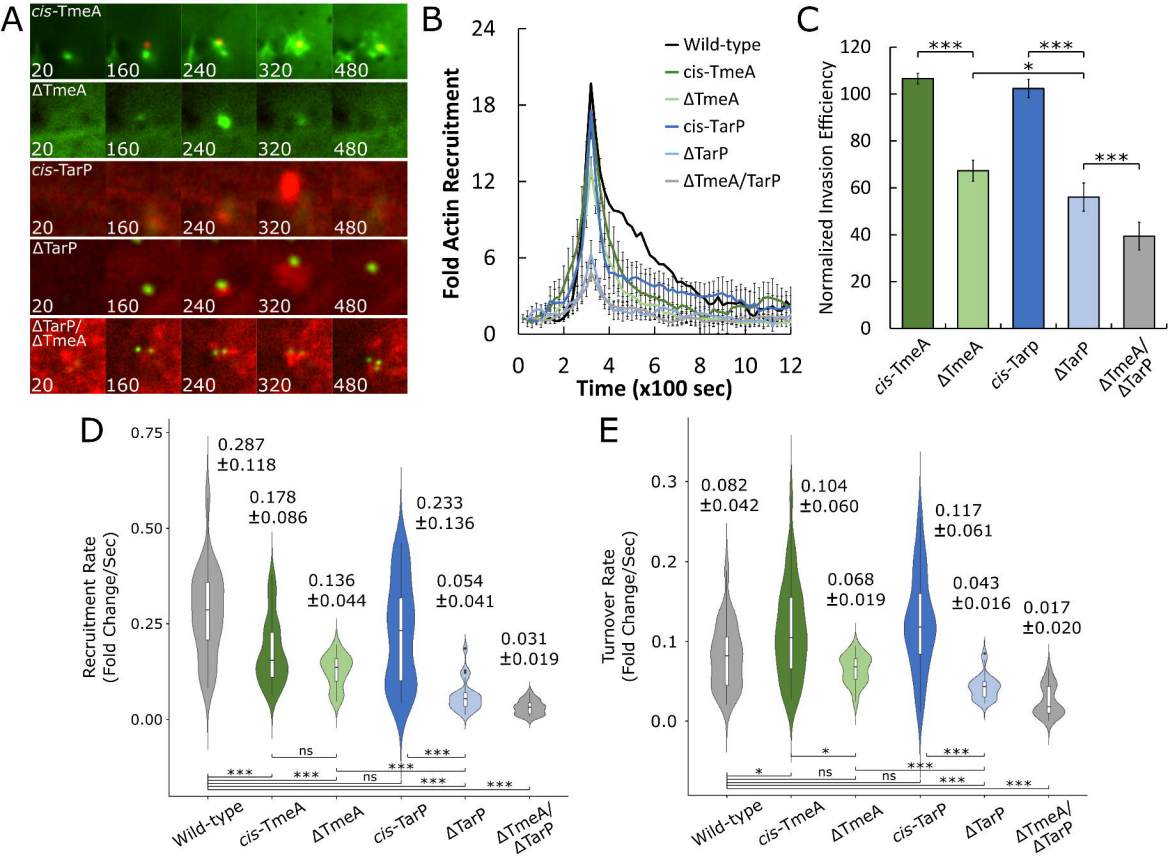
A
cis-TmeA
ΔTmeA
cis-TarP
ΔTarP
ΔTarP/ ΔTmeA
20
160
240
320
480
B
Fold Actin Recruitment
Time (x100 sec)
Wild-type
cis-TmeA
ΔTmeA
cis-TarP
ΔTarP
ΔTmeA/TarP
C
Normalized Invasion Efficiency
cis-TmeA
ΔTmeA
cis-Tarp
ΔTarP
ΔTmeA/ ΔTarP
D
Recruitment Rate (Fold Change/Sec)
0.287 ±0.118
0.178 ±0.086
0.136 ±0.044
0.233 ±0.136
0.054 ±0.041
0.031 ±0.019
E
Turnover Rate (Fold Change/Sec)
0.082 ±0.042
0.104 ±0.060
0.068 ±0.019
0.117 ±0.061
0.043 ±0.016
0.017 ±0.020
Wild-type
cis-TmeA
ΔTmeA
cis-TarP
ΔTarP
ΔTmeA/ ΔTarP

# Figure 2

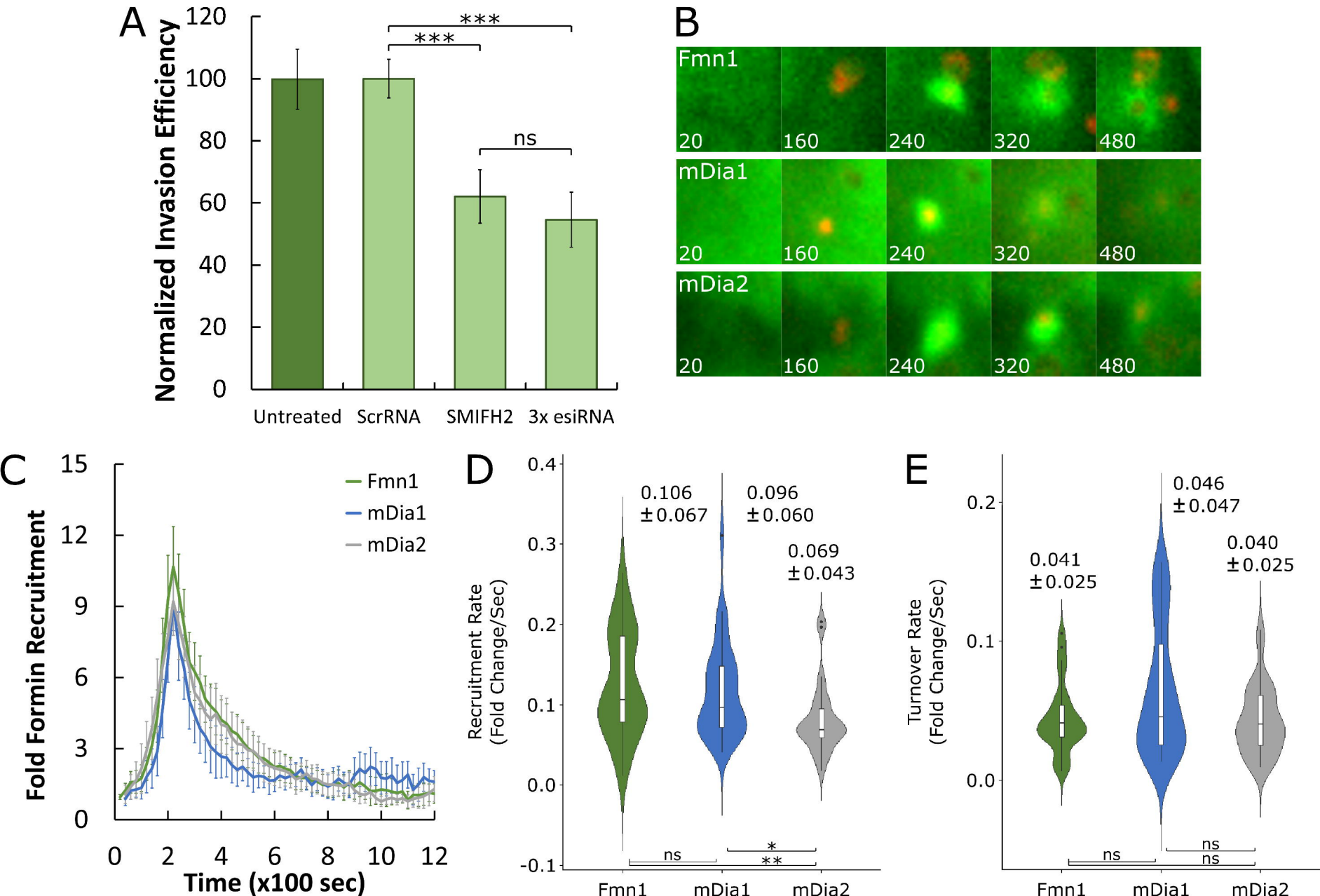
A
Normalized Invasion Efficiency
120
100
80
60
40
20
0
***
***
ns
Untreated
ScrRNA
SMIFH2
3x esiRNA
B
Fmn1
mDia1
mDia2
20
160
240
320
480
C
Fold Formin Recruitment
Time (x100 sec)
Fmn1
mDia1
mDia2
D
Recruitment Rate
(Fold Change/Sec)
0.106
±0.067
0.096
±0.060
0.069
±0.043
ns
*
**
E
Turnover Rate
(Fold Change/Sec)
0.041
±0.025
0.046
±0.047
0.040
±0.025
ns
ns
ns

# Figure 3

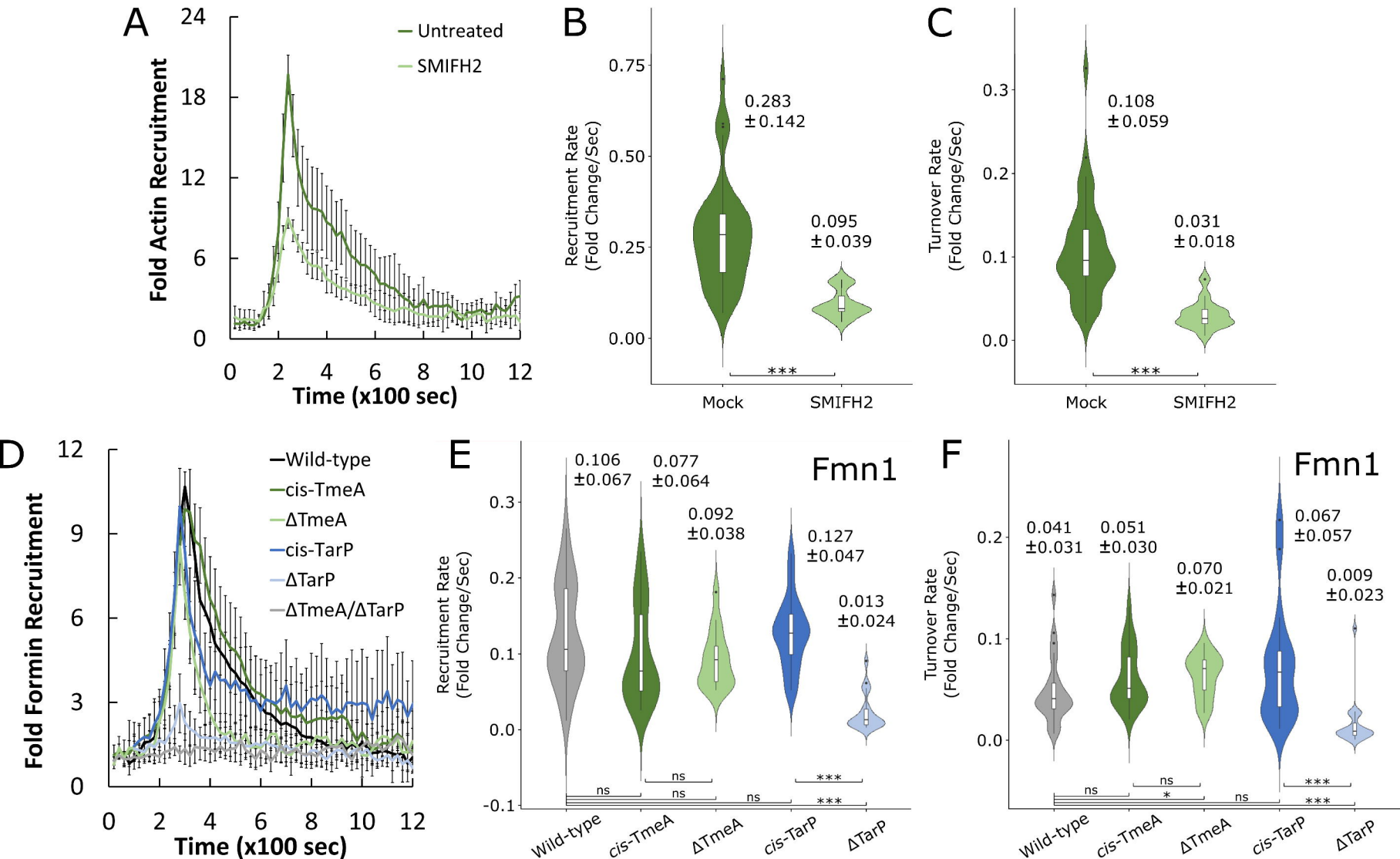
A
Untreated
SMIFH2
Fold Actin Recruitment
Time (x100 sec)
B
Recruitment Rate (Fold Change/Sec)
0.283 ±0.142
0.095 ±0.039
***
Mock
SMIFH2
C
Turnover Rate (Fold Change/Sec)
0.108 ±0.059
0.031 ±0.018
***
Mock
SMIFH2
D
Wild-type
cis-TmeA
ΔTmeA
cis-TarP
ΔTarP
ΔTmeA/ΔTarP
Fold Formin Recruitment
Time (x100 sec)
E
Fmn1
Recruitment Rate (Fold Change/Sec)
0.106 ±0.067
0.077 ±0.064
0.092 ±0.038
0.127 ±0.047
0.013 ±0.024
ns
ns
ns
ns
***
***
Wild-type
cis-TmeA
ΔTmeA
cis-TarP
ΔTarP
F
Fmn1
Turnover Rate (Fold Change/Sec)
0.041 ±0.031
0.051 ±0.030
0.070 ±0.021
0.067 ±0.057
0.009 ±0.023
ns
ns
*
ns
***
***
Wild-type
cis-TmeA
ΔTmeA
cis-TarP
ΔTarP

# Figure 4

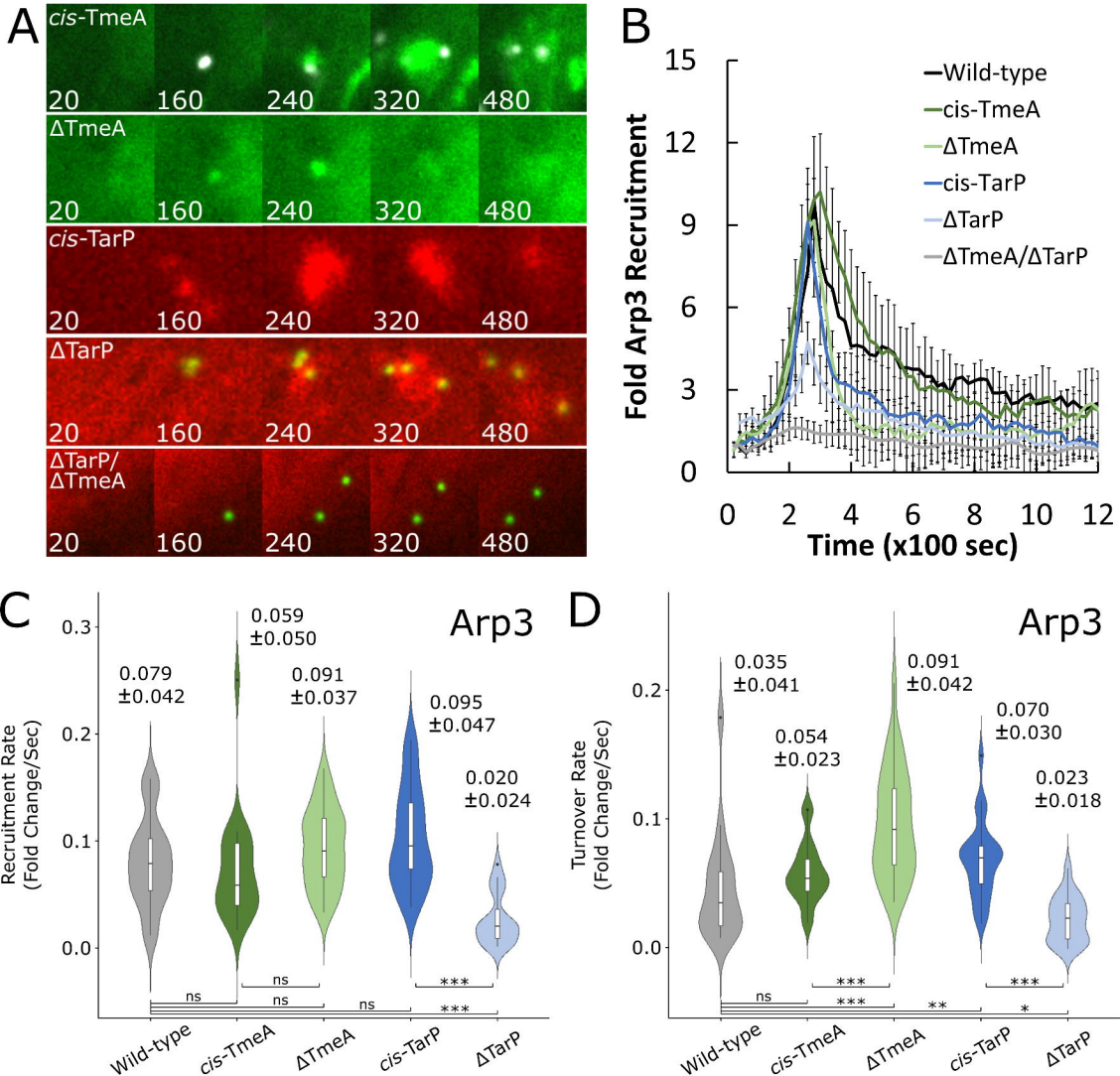
A
cis-TmeA
ΔTmeA
cis-TarP
ΔTarP
ΔTarP/ ΔTmeA
20
160
240
320
480
B
Fold Arp3 Recruitment
Time (x100 sec)
Wild-type
cis-TmeA
ΔTmeA
cis-TarP
ΔTarP
ΔTmeA/ΔTarP
C
Arp3
Recruitment Rate (Fold Change/Sec)
0.079 ±0.042
0.059 ±0.050
0.091 ±0.037
0.095 ±0.047
0.020 ±0.024
ns
***
Wild-type
cis-TmeA
ΔTmeA
cis-TarP
ΔTarP
D
Arp3
Turnover Rate (Fold Change/Sec)
0.035 ±0.041
0.054 ±0.023
0.091 ±0.042
0.070 ±0.030
0.023 ±0.018
ns
***
**
*

# Figure 5

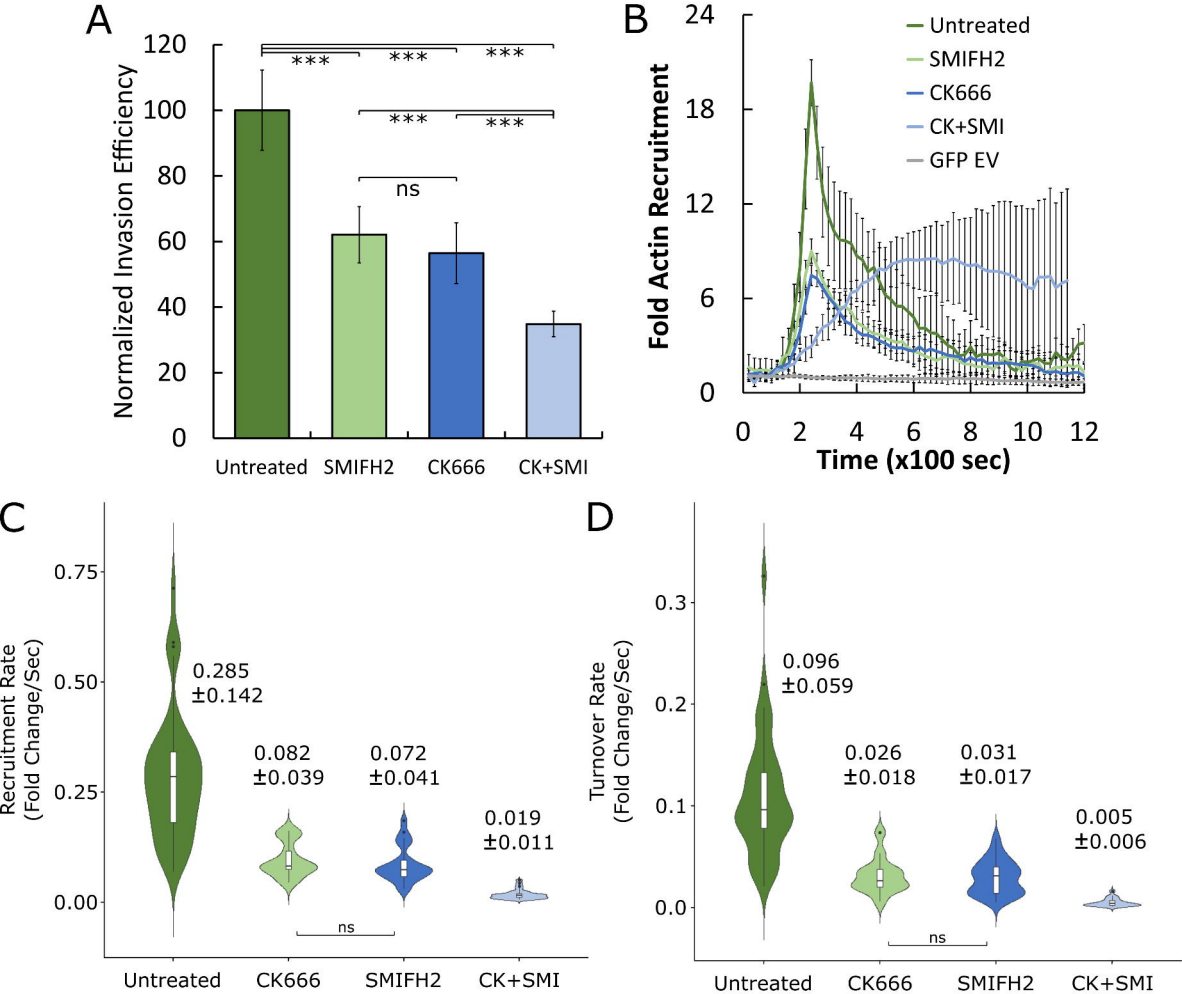
A
Normalized Invasion Efficiency
120
100
80
60
40
20
0
***
***
***
***
***
ns
Untreated
SMIFH2
CK666
CK+SMI
B
Fold Actin Recruitment
24
18
12
6
0
Untreated
SMIFH2
CK666
CK+SMI
GFP EV
0
2
4
6
8
10
12
Time (x100 sec)
C
Recruitment Rate
(Fold Change/Sec)
0.75
0.50
0.25
0.00
0.285
±0.142
0.082
±0.039
0.072
±0.041
0.019
±0.011
ns
Untreated
CK666
SMIFH2
CK+SMI
D
Turnover Rate
(Fold Change/Sec)
0.3
0.2
0.1
0.0
0.096
±0.059
0.026
±0.018
0.031
±0.017
0.005
±0.006
ns
Untreated
CK666
SMIFH2
CK+SMI

# Figure 6

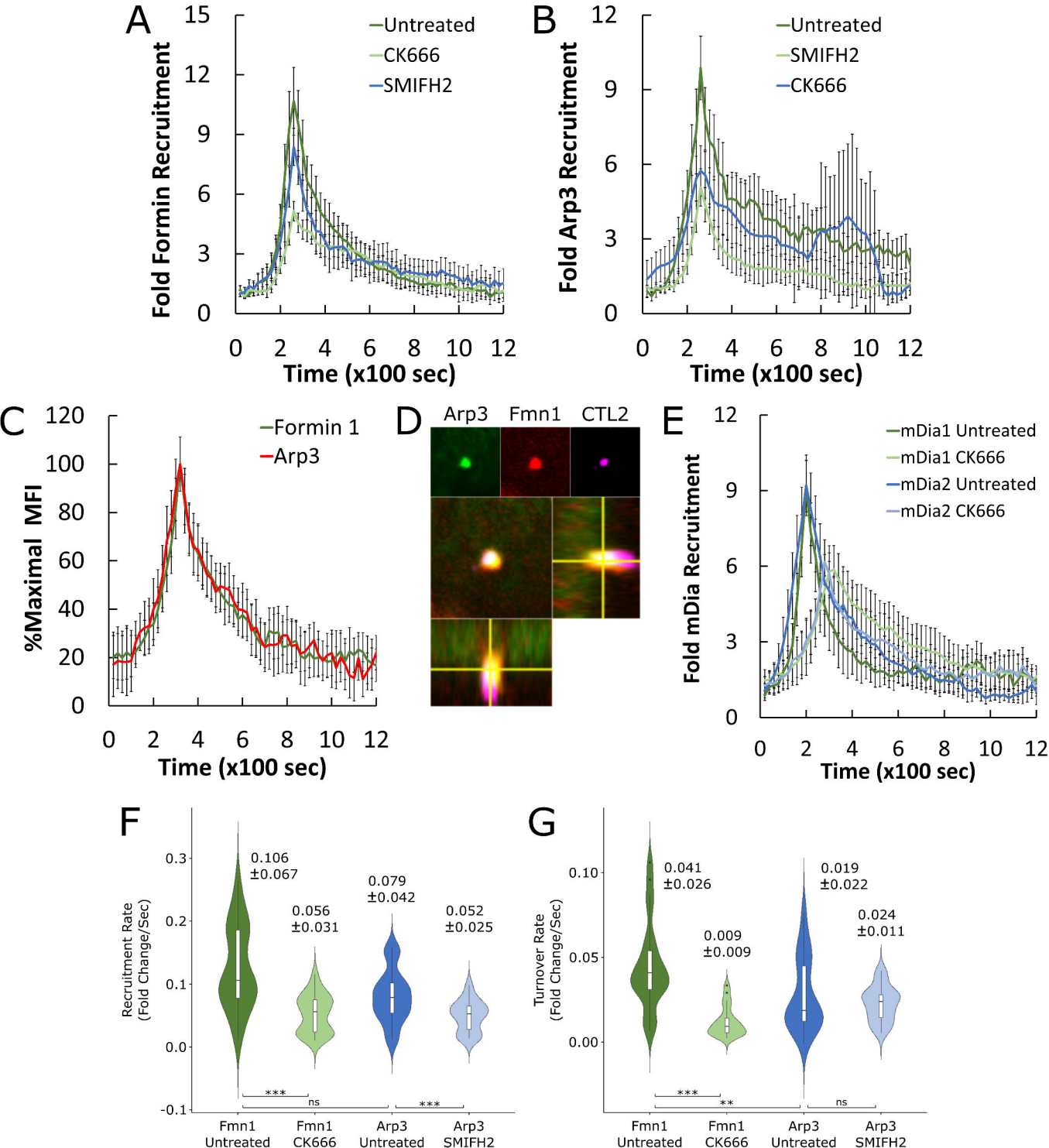
A
Fold Formin Recruitment
Untreated
CK666
SMIFH2
Time (x100 sec)
B
Fold Arp3 Recruitment
Untreated
SMIFH2
CK666
Time (x100 sec)
C
%Maximal MFI
Formin 1
Arp3
Time (x100 sec)
D
Arp3
Fmn1
CTL2
E
Fold mDia Recruitment
mDia1 Untreated
mDia1 CK666
mDia2 Untreated
mDia2 CK666
Time (x100 sec)
F
Recruitment Rate (Fold Change/Sec)
0.106 ±0.067
0.056 ±0.031
0.079 ±0.042
0.052 ±0.025
***
ns
***
Fmn1 Untreated
Fmn1 CK666
Arp3 Untreated
Arp3 SMIFH2
G
Turnover Rate (Fold Change/Sec)
0.041 ±0.026
0.009 ±0.009
0.019 ±0.022
0.024 ±0.011
***
**
ns
Fmn1 Untreated
Fmn1 CK666
Arp3 Untreated
Arp3 SMIFH2

Figure 7

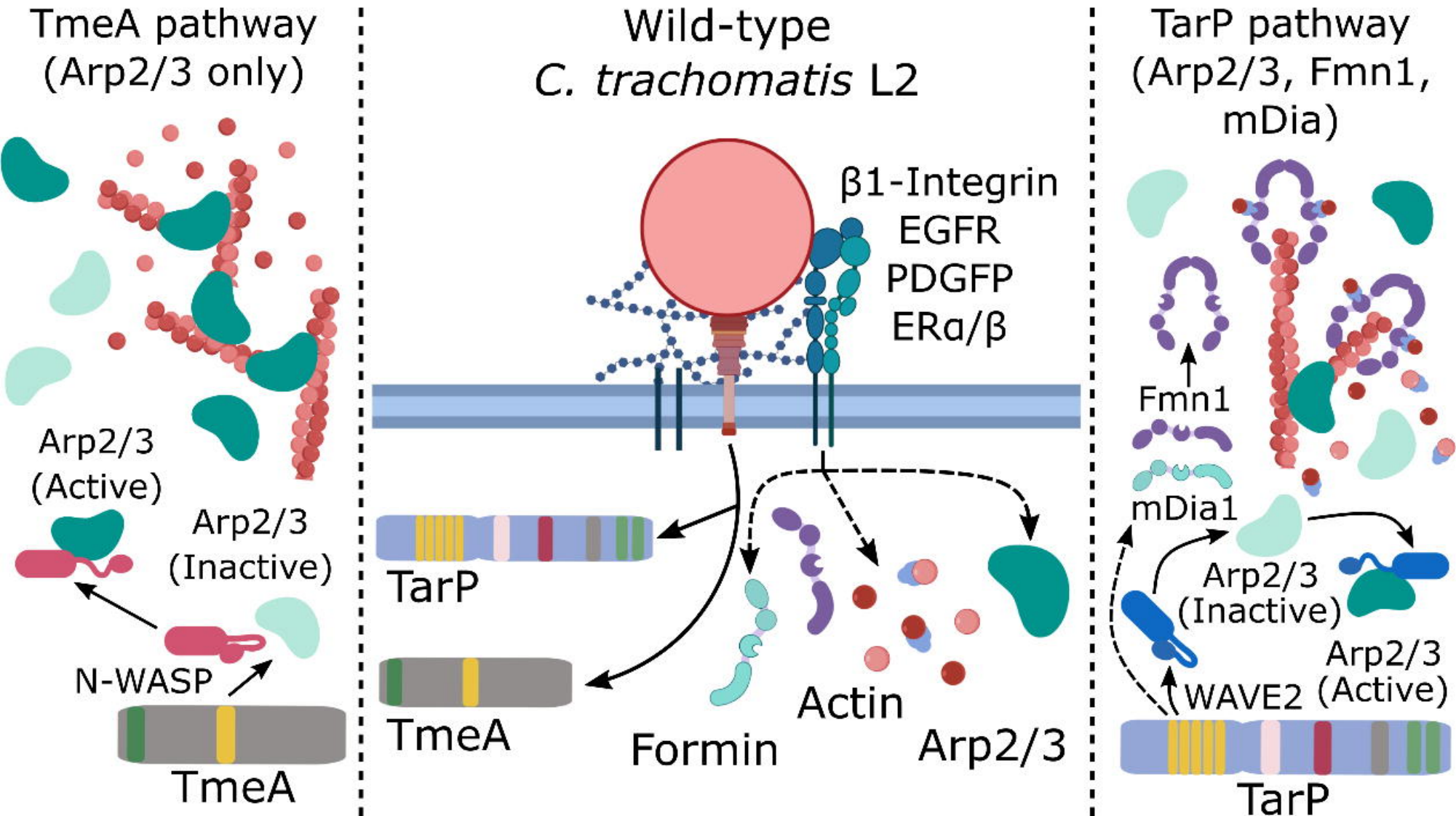
TmeA pathway
(Arp2/3 only)
Arp2/3
(Active)
Arp2/3
(Inactive)
N-WASP
TmeA
Wild-type
C. trachomatis L2
β1-Integrin
EGFR
PDGFP
ERα/β
TarP
TmeA
Formin
Actin
Arp2/3
TarP pathway
(Arp2/3, Fmn1,
mDia)
Fmn1
mDia1
Arp2/3
(Inactive)
Arp2/3
(Active)
WAVE2
TarP